

Unscrambling light scattering to enable deep tissue optical imaging: a computational investigation

Jake Bewick

A dissertation submitted in partial fulfillment
of the requirements for the degree of
Master of Research
of
University College London.

Department of Medical Physics and Biomedical Engineering
University College London

September 27, 2020

I, Jake Bewick, confirm that the work presented in this thesis is my own. Where information has been derived from other sources, I confirm that this has been indicated in the work.

Abstract

The delivery of coherent light into biological tissue is critical for numerous imaging and treatment modalities. Unfortunately, tissue is highly scattering. As a consequence, coherence is quickly lost and most of these modalities have a limited effective depth. However, by spatially modulating the incident light we are able to guide its propagation through a turbid medium, effectively unscrambling light scattering and enabling deep tissue imaging. The process of engineering this spatially modulated wave is known as wavefront shaping.

Wavefront shaping is still a nascent technique, the understanding of which has been constrained by various experimental limitations. Researchers have limited control over the design of a scattering medium, and are unable to easily image the propagating light inside this medium. Instead, a new approach based on computational modelling would be necessary to fully understand wavefront shaping.

In this thesis we propose two separate models capable of simulating wavefront shaping: an angular spectrum approach which simulates scattering using refractive index variations, and a T-Matrix method that uses discrete spherical particles to represent tissue. We find that the angular spectrum method is efficient, but unable to fully characterise the optical properties of biological tissue. The T-Matrix method is better in this regard, and shows promise as a novel way to study wavefront shaping.

Acknowledgements

I would like to thank my three supervisors, Jamie Guggenheim, Peter Munro, and Simon Arridge for their continued support and advice over the past (uniquely disruptive) year.

Contents

1	Introduction	11
1.1	Problem Statement	11
1.1.1	What is wavefront shaping?	11
1.1.2	Applying computational modelling to wavefront shaping. . .	12
1.2	Project Applications	13
1.3	In this Thesis	14
2	Background	16
2.1	Principles and Practice of Wavefront Shaping	16
2.1.1	Spatial modulation of light	16
2.1.2	Determining the correct phase and/or amplitude map	17
2.1.3	Applications of Wavefront Shaping	21
2.2	Models of Light Propagation in Tissue	29
2.2.1	Light Scattering by Biological Tissues	29
2.2.2	Tissue Optical Properties	29
2.2.3	Continuum Model	30
2.2.4	Discrete Particle Model	30
2.3	Computational Electromagnetics	31
2.3.1	FDTD, FEM and BEM	31
2.3.2	The Monte-Carlo Method	34
2.3.3	The Discrete Dipole Approximation	35
2.3.4	The Angular Spectrum Method	36
2.3.5	The T-Matrix Method	36

2.3.6	Requirements of a Wavefront Shaping Model	37
3	Methods	40
3.1	The Two Models	40
3.2	Mathematical Theory	41
3.2.1	The Angular Spectrum Method	42
3.2.2	The T-Matrix Method	43
3.3	Generating the Model Domain	47
3.3.1	Angular Spectrum and the Continuum Model	47
3.3.2	T-Matrix and the Discrete Particle Model	48
3.4	Scaling within MSTM	51
3.5	Validation	52
3.5.1	Diffraction Patterns with the Angular Spectrum Method	52
3.5.2	Single Sphere Simulation	53
3.5.3	Scattering Simulations in MSTM	53
3.6	Speckle Generation with the T-Matrix	55
4	Results	56
4.1	The Angular Spectrum Method	56
4.1.1	Diffraction Patterns	56
4.1.2	Binary Amplitude and Phase Modulation	57
4.2	The T-Matrix Method	59
4.2.1	Generating Discrete Particle Models	59
4.2.2	Scaling with MSTM	61
4.3	IAD Validation	63
4.4	Speckle Generation	66
5	Discussion	68
5.1	The Angular Spectrum Method	68
5.1.1	Diffraction Patterns	68
5.1.2	Binary Amplitude and Phase Modulation	69
5.2	The T-Matrix Method	70

	<i>Contents</i>	<i>7</i>
5.2.1	Scaling with MSTM	70
5.3	IAD Validation	71
5.4	Speckle Generation	73
6	Conclusion	74
	Bibliography	76

List of Figures

1.1	Wavefront shaping uses shaped beams to generate a focus through a turbid medium.	15
3.1	Scattering coefficient and anisotropy as a function of wavelength, as determined by Lorenz-Mie theory.	51
3.2	Measurements Inverse Adding Doubling needs to determine the optical properties of a scattering medium.	54
4.1	Fresnel diffraction of a plane wave through a circular aperture. . . .	56
4.2	Fresnel diffraction of a plane wave that is obstructed a circular aperture.	57
4.3	Scattered light calculated with the angular spectrum method.	58
4.4	Binary amplitude and phase focuses generated using the stepwise sequential algorithm and simulated with the angular spectrum method.	58
4.5	Generating discrete particle domains for use with T-Matrix methods.	60
4.6	Creating differently sized multi-sphere domains to investigate scaling using the T-Matrix method.	61
4.7	Temporal scaling behaviour of MSTM	62
4.8	Determining the optimum radius and depth for a disk shaped scatterer.	63
4.9	The discrete particle model used for IAD simulation.	64
4.10	The transmittance, reflectance and ballistic profile for a Gaussian beam incident on a scattering medium calculated using MSTM.	64
4.11	Near field intensity along the longitudinal plane for different scattering domains.	65

List of Figures

9

4.12 Speckle patterns generated with MSTM.	67
4.13 Histogram plot of the speckle pattern generated using only 500 spheres.	67

List of Tables

2.1	Maximum enhancement achievable using various spatial modulation methods.	17
2.2	Explanation of the different wavefront shaping optimisation algorithms.	19
2.3	Applications of wavefront shaping.	22
2.4	Common, rigorous, methods in computational electromagnetics.	32
4.1	Focus enhancement for binary amplitude or phase modulation simulated using the angular spectrum method.	59
4.2	Optical properties of our simulation as determined by Mie theory, IAD and MSTM.	66

Chapter 1

Introduction

1.1 Problem Statement

1.1.1 What is wavefront shaping?

Many biomedical applications rely on the delivery of light into biological tissue for diagnostic and therapeutic purposes [1]. However, biological tissue contains many refractive index inhomogeneities, which strongly scatters incident light [2] and prevents deep tissue penetration. Coherence of the incident light is also quickly lost due to multiple scattering.

Fortunately, scattering is a deterministic and effectively reversible process - a spatially modulated wavefront can be engineered to generate a desired field either inside or through a turbid medium. For example, by spatially steering an incident wave an optical focus can be generated through a heavily scattering material (see Figure 1.1).

In a single sentence: wavefront shaping (WFS) is the process by which light can be spatially modulated to control how the scattered light interacts. This allows for deeper tissue imaging with improved resolution and contrast [3] (other applications of WFS will be discussed at detail later in the report).

1.1.2 Applying computational modelling to wavefront shaping.

The vast majority of literature on wavefront shaping has been experimentally based. The absence of computational research may be due to the difficulty of modelling light propagation through turbid media - scattering is a micro-scale process occurring throughout the entire volume of a macro-scale tissue, and as such most simulation techniques are prohibitively difficult to run.

Nevertheless, there is a need to model wavefront shaping computationally. An experimental approach is unable to evaluate the field inside the scattering medium, instead relying on two different metrics to assess focus generation:

- If WFS is used to create a focus through a turbid medium the output field can be imaged directly [4].
- If WFS is used to create a focus inside a turbid medium other feedback mechanisms must be used to evaluate the localised increase in light intensity (e.g. using a fluorescent bead, or photoacoustic signal [5]). These non-direct measurements of intensity can be considered analogous to the guidestars used in adaptive optics.

Both methods are insufficient in fully charactering the generated focus, or the path light takes to generate this focus. Many unanswered questions remain that cannot easily be explored experimentally:

- If WFS through a medium, what is the 3D geometry of the focus? A 2D image is unable to characterise whether the focus is tightly localised or more oblate in shape.
- If WFS inside a medium, where is the focus actually located? Determining a correct spatial position is limited by the resolution of the feedback mechanism used for shaping.
- For both methods, what is happening inside the scattering medium? Although unlikely, it may be entirely possible that multiple foci have been unintentionally generated.

Another motivation behind computationally simulating wavefront shaping is the ability to have complete control over all simulation parameters. Carefully designed scatterers can be deliberately placed to form a unique turbid medium. Additionally, the incident wavefront can be more freely shaped and tissue parameters such as the scattering coefficient and anisotropy can be specifically controlled.

A recent work by Yang *et al.* (and one of the only attempts to simulate WFS) has investigated the effect camera signal-to-noise ratio, guidestar size and spatial light modulator geometry have on focus generation, factors that would be difficult to control for experimentally [6].

1.2 Project Applications

The applications of computationally modelling wavefront shaping will (hopefully) become more clear when reading the report. They are nevertheless stated early to act as a reference for the reader, and establish a clear motivation for the project.

- *How does shaped light propagate through a scattering medium?* Computational modelling allows us to evaluate the field throughout the medium, and as such it is the only way to completely characterise the physics of wavefront shaping.
- *What impact do different biological tissues have?* Experimental studies on wavefront shaping have used an interesting mix of tissue, or tissue-like materials. Foci have been generated through titanium dioxide paint [7], ground glass diffusers [7], chicken breast [8], a mouse tail [9], and even a human tooth [4]. It may also be worth considering the effect that the clearing agents used for optical coherence tomography would have on WFS [10].
- *How does the method of shaping light effect light propagation?* An optical wavefront can be shaped using either phase or amplitude modulation, and this modulation can either be binary or continuous. The maximum possible enhancement of each method has been determined theoretically, but experimentally reported values are 10-30% lower than predicted [11]. Yu *et al.* suggest

that this variation is likely caused by experimental limitations, such as vibration causing decorrelation, or temperature fluxuations [11] - all confounding factors that can be controlled for computationally.

- *What impact does noise have?* The noise introduced by various experimental apparatus can be easily simulated. As previously mentioned, Yang *et al.* have already investigated the effect detector signal-to-noise ratio has on focus generation.
- *What is the best procedure for modelling wavefront shaping through biological tissue?* Very few attempts have been made to computationally model wavefront shaping. As of yet, no researcher has undertaken a critical review of existing scattering models with the goal to evaluate their suitability for wavefront shaping.
- *What are the limits of the optical memory effect?* Light propagation through biological tissue is shift invariant - a small variation in the angle of the incident wave does not result in decorrelation [12]. To date, there has been no computation investigation of this phenomena.

1.3 In this Thesis

The overarching goal of this thesis is to identify and evaluate computational models of wavefront shaping. We start by explaining the principles and practice of wavefront shaping, before describing how light propagates through tissue, and the different ways to model this propagation. We then introduce some conventional and unconventional computation models, before identifying the two models would be best suited to simulate wavefront shaping: the angular spectrum approach and the T-Matrix method. We critically evaluate the models and describe the mathematical background of each. We then describe how biological tissue can be resresented in each model, before performing various light propagation simulations. We conclude by critically evaluating the results of these simulations, and describe what we think would be the best applications for each model.

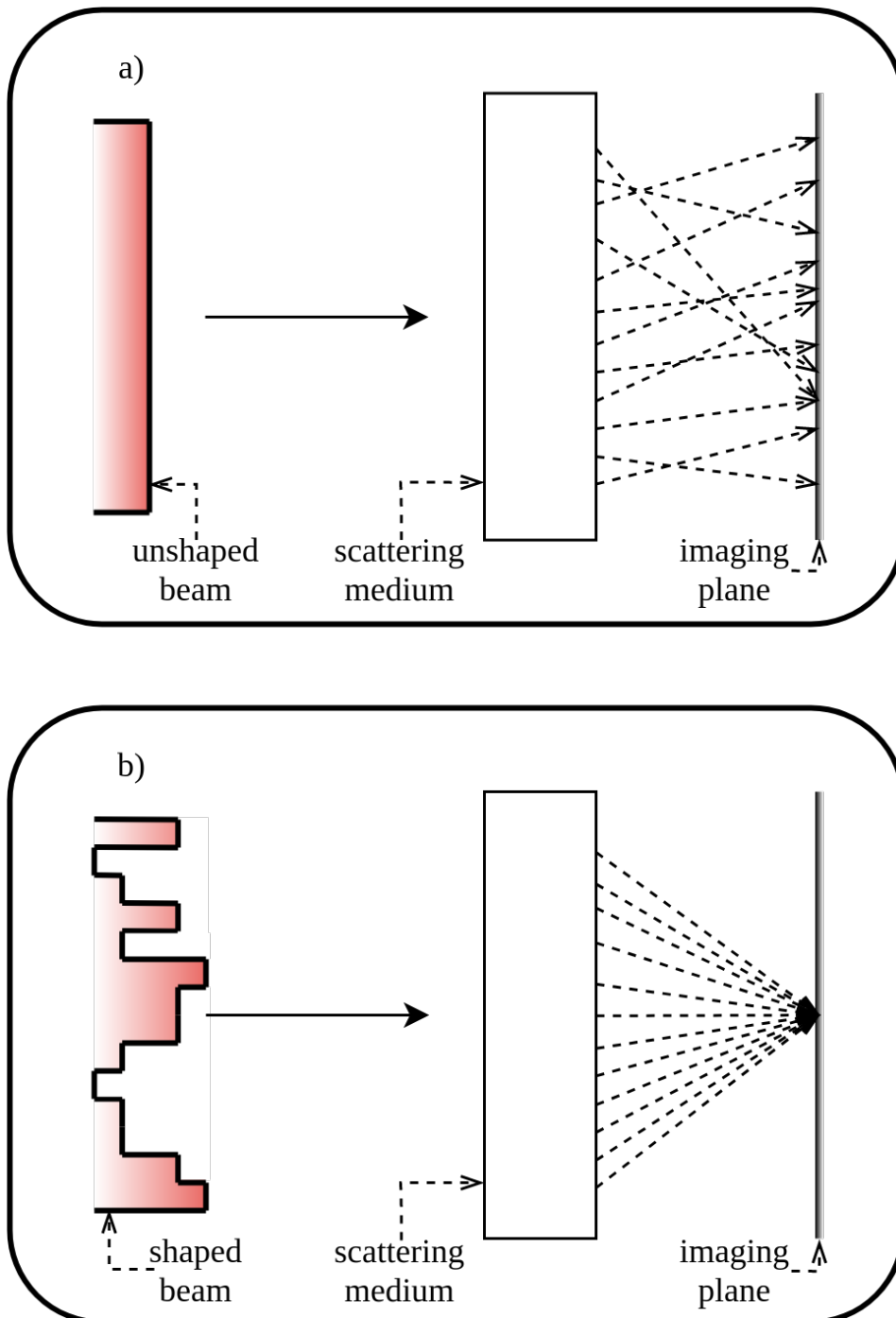


Figure 1.1: A demonstration of wavefront shaping. In a) coherent light incident on a turbid medium is scattered, and would produce a speckle pattern on the imaging plane. By spatially modulating the incident wavefront, as shown in b), it becomes possible to guide the propagating light through the scatterer, generating an optical focus.

Chapter 2

Background

2.1 Principles and Practice of Wavefront Shaping

2.1.1 Spatial modulation of light

As previously mentioned, wavefront shaping is the process of spatially modulating light to guide propagation through a scattering medium.

In WFS, a wavefront is subdivided into many elements, by modifying the phase or amplitude of individual elements the propagation of light through a scattering medium can be controlled. These phase or amplitude shifts are applied using a family of optical devices called wavefront modulators, examples of which include spatial light modulators (SLM) and digital micro-mirror devices (DMD). Each device varies in operation and as such has unique advantages and disadvantages: for example, a DMD is generally faster and has a higher element count than a SLM, but has a lower diffraction efficiency and is less suited to phase modulation [11].

Both amplitude and phase modulation can either be binary or more graded. The specific method of modulation determines the maximum possible enhancement, η , with full phase and amplitude control achieving an enhancement of [13]:

$$\eta_{\text{pred}} = \alpha(N - 1) + 1 \quad (2.1)$$

where N is the number of elements used to control modulation and α represents an enhancement factor that can be used to characterise the efficiency of other modulation methods (see Table 2.1).

Table 2.1: Maximum possible enhancement for different spatial modulation methods. Data taken from Vellekoop *et al.* [14]

Modulation Method	α
Full phase	$\pi/4$
Binary amplitude	$1/2\pi$
Binary phase	$1/\pi$

2.1.2 Determining the correct phase and/or amplitude map

There are two primary methods for determining the correct phase and/or amplitude map for a given wavefront modulator: iterative methods and digital optical phase conjugation (DOPC) methods.

Iterative methods shape a wavefront gradually using feedback mechanisms. For example, to generate an optical focus, a feedback based mechanism might iterate through each element on an SLM, shifting the phase between 0 and 2π while measuring the resultant intensity change within a region of interest [4].

Measuring intensity is trivial if shaping through a turbid medium, the focal plane can be projected directly onto a CCD [14]. However, when generating a focus inside a scattering medium, direct measurement of intensity becomes impossible. Instead guidestar based methods must be used [5].

In wavefront shaping, guidestars provide an indirect measurement of the field inside a scattering medium. For the simplest example: a nanoscale fluorescent bead is embedded within a turbid medium. By measuring the amount of excited light generated during wavefront shaping, you would have an indirect measure of how effectively incident light is being focused onto a the bead [15].

Guidestars do not have to be physical beads - non-invasive alternatives include measuring the strength of the ultrasound signal generated via the photoacoustic effect [16], or detecting a two-photon fluorescence signal [17].

In general, iterative methods are slow - limited by both optimisation algorithm time and light modulator speed. This slow speed of focus generation currently limits feedback based WFS techniques from being applied in dynamic biological tissues [18], although recent developments have dramatically increased SLM speed [19].

Optimisation algorithm development has also significantly increased the speed of iterative approaches [20]. For a brief explanation and evaluation of four popular algorithms see Table 2.2.

Table 2.2: The various optimisation algorithms used in wavefront shaping. For a more comprehensive comparison of different algorithms see the following two papers both by Fayyaz et al. [21, 20].

Optimisation algorithm	Explanation	Comments
Stepwise sequential	In sequential optimisation, the phase or amplitude of each element is independently modulated. The modulation which provides the largest increase in intensity for a given element is stored, and the final mask is simply a combination of each optimised element [22].	Sequential optimisation is eventually guaranteed to find the optimal phase or amplitude map. Unfortunately, it is very slow, and struggles with noise [20].
Partition	Half of the elements are randomly selected and simultaneously optimised for phase and/or amplitude. The algorithm then repeats with another set of elements being randomly selected [23].	As multiple channels are optimised in parallel, intensity under the partition algorithm grows much faster initially, but quickly slows as the number of iterations increases [20].
Transmission matrix	Transmission matrix methods fully characterise the scattering behaviour of a medium for a given incident wave. After varying the phase of the n^{th} SLM element by either $0, \pi/2, \pi$, or $3\pi/2$ you measure the intensity of the m^{th} output channel [24]. The transmission matrix elements, t_{mn} , can then be found using the following equation [20]: $t_{mn} = [(I_m^0 - I_m^\pi)/4] + i[(I_m^{3\pi/2} - I_m^{\pi/2})/4]$.	Solving the transmission matrix allows for a focus to be generated anywhere within the medium. This approach suffers from the same downside as the sequential method - each input channel is evaluated independently, making the algorithm very susceptible to the influence of noise [20]. Another downside is the requirement to measure the intensity across the entire output field, meaning transmission matrix methods struggle to be used to generate foci inside a scattering medium.
Genetic algorithms	In the genetic algorithm approach a random phase and/or amplitude map is generated and evaluated. The random maps that produce the greatest focus intensity are “bred” and then “mutated” - meaning they are combined after applying a binary mask and a few elements are randomly shifted [25]. The lower scoring maps are then deleted and the algorithm repeats.	Genetic algorithms have two primary advantages: they converge to a relatively high intensity quickly [25] and they are the most resistant to noise [20]

The second approach to shaping a wave is called digital optical phase conjugation (DOPC). DOPC methods exploit the fact that scattering is deterministic and time-reversible - a phase conjugated scattered wavefront should retake the exact same trajectory as the original scattered wave [26]. If this scattered light first originated from a focus either inside or behind a turbid medium, than an incident, phase conjugated wavefront would naturally create the same focus.

Holographically measuring the phase conjugated scattered light generated by a focus on the other side of a turbid medium is the simplest implementation of DOPC [27]. However, it is difficult to generate the focus needed to produce the phase conjugated wavefront from inside a scatterer. A series of solutions have been created to internally generate this focused signal.

One approach centres around implanting either a nanoparticle [28] or fluorescent bead [29] into the scattering medium, and measuring the generated second-harmonic or fluorescent signal respectively. Although simple, these methods are invasive when applied to biological tissue, and the focus point cannot be shifted dynamically.

To allow for dynamic control of the focal point inside the tissue, the time-reversed magnetically controlled perturbation (TRMCP) technique may be applied [30]. This method works by detecting the absorption of light from a magnetic microsphere and phase conjugating this light back into the tissue. The authors suggest that the location of this particle may be controlled externally using a magnetron, allowing for dynamic focusing. However, these methods are all invasive, and instead it may be worth considering solutions that use a virtual guidestar for WFS.

An example of this is time-reversed ultrasonically encoded (TRUE) focusing. TRUE focusing exploits the phenomena by which ultrasound is capable of modulating the frequency of diffuse light [31]. If this ultrasound is focused inside a

turbid medium, it would be possible to phase conjugate only the frequency shifted light to produce an acoustic diffraction limited spot [32].

To overcome this acoustic diffraction size limitation researchers have proposed two newer methods: time reversal of variance-encoded light (TROVE) and time-reversal ultrasound microbubble encoded light (TRUME). In TROVE, multiple input fields are all ultrasonically frequency shifted, the variance between these shifted wavefronts is decoupled, producing a speckle sized focus [33]. In TRUME the ultrasonic destruction of individual microbubbles is used to encode light, producing a microbubble sized focus [34].

Virtual guidestars are also able to focus on moving targets, which may have applications for flow cytometry and blood monitoring [5]. The time-reversed adapted-perturbation [35] (TRAP) method and time reversal by analysis of changing wavefronts from kinetic targets [36] (TRACK) method both create an optical focus by holographically recording the scattered field of a moving target at two locations - the conjugated difference in fields can then be used to focus light onto the moving target [5].

2.1.3 Applications of Wavefront Shaping

WFS allows for deeper coherent light penetration into tissue, and as such has the potential to directly benefit many biomedical imaging and treatment modalities. A comprehensive evaluation of the applications of WFS can be found in Table 2.3.

Table 2.3: Applications of wavefront shaping.

Imaging			
Modality	Description	WFS Benefits	Example applications
Photoacoustic Imaging	<p>Pulsed laser light causes biological tissue to generate ultrasonic waves via the photoacoustic effect, these sound waves can then be detected by surface transducers [37]. Compared to ultrasound, photoacoustic imaging has a higher resolution and greater specificity (as different wavelengths of light are more efficiently absorbed by specific chromophores). There are two varieties of photoacoustic imaging: photoacoustic tomography and microscopy. In photoacoustic tomography, scattering causes tissue to be bathed in diffuse light, and inverse algorithms are needed to reconstruct the image from detected signals [38]. Optical resolution photoacoustic microscopy instead uses a focused laser beam to spatially constrain the origin of the ultrasonic signal, and as such no reconstruction algorithm is necessary [39]. The need for spatial focusing limits this modality to superficial tissues, approximately 1mm [1].</p>	<p>WFS can increase imaging depth for photoacoustic microscopy by creating an optical focus inside a turbid scattering medium. In doing so WFS can produce photoacoustic images with a higher resolution and signal-to-noise ratio [40].</p>	<p>Lai <i>et al.</i> have exploited the Grueneisen memory effect to generate a nonlinear photoacoustic signal that allows for optical focusing smaller than the acoustic diffraction limit, producing images with a higher signal-to-noise ratio [41]. Similarly, Conkey <i>et al.</i> also generate a sub-acoustic diffraction limit focus and are able to produce high resolution images of an alpaca hair and bee wing [40]. One limitation of these nonlinear techniques is the inability to control where focus emerges within the limits of acoustic diffraction. Another approach is taken by Chaigne <i>et al.</i>, who do not use an iterative optimisation algorithm, instead determining the photoacoustic transmission matrix of a medium to generate a focus [42]. One major advantage of transmission matrix shaping approaches is the ability to investigate the impact of each SLM pixel on multiple output modes, while iterative methods only use a single output point the measured signal [43].</p>

Optical coherence tomography

Optical coherence tomography (OCT) is a high resolution ($< 10\mu m$), low depth (about $1mm$, although this is much greater than most other optical methods) imaging technique most commonly used for retinal imaging [44]. In OCT the backscattered light from tissue is used as the contrast for imaging [45]. The speed of light is too fast to directly measure time-of-flight information from the backscattered light, instead low-coherence interferometry is used to provide axial information [46]. It is important to note that the imaging contrast from OCT comes only from singly backscattered light [47] - multiply scattered light reduces contrast, resolution and penetration depth [48].

By shaping the incident light, WFS can cause multiply scattered light to interfere, producing an optical focus inside a turbid tissue. This increases the signal-to-noise ratio and effective penetration depth.

Yu *et al.* have used binary amplitude modulation to focus light into a fibrin phantom for OCT, reaching a maximum increase in penetration depth of 92% [49]. They later apply the same method on biological tissue (a mouse tail) and similarly find that increased imaging depth is possible with WFS [47]. The increase in penetration is smaller for the biological mouse tail due to the faster decorrelation time. Interestingly, one of the only WFS simulations has been performed for OCT - with Kim *et al.* simulating the benefits of WFS on OCT [50]. Prior to this work only “*indirect evidence*” [50] of the effect of WFS on OCT was available as it is practically impossible to measure the complete internal field of a turbid medium. The researchers use the finite-difference time-domain method, which (as the name suggests) is a time-domain method, and as such is well suited to modelling OCT, which uses low-coherence light.

Light sheet fluorescence microscopy	<p>Light sheet fluorescence microscopy (LSFM) is an imaging technique, unique in that the target tissue is illuminated perpendicularly with a very thin plane of light [53]. As only a narrow slice is illuminated, LSFM is very effective at transverse sectioning of samples, producing high contrast images (in conventional confocal microscopy the unfocused background is also illuminated, reducing contrast [54]).</p>	<p>Ideally, the light sheet should remain ballistic when propagating through target tissue, such that nothing in the background is illuminated [54]. WFS can be used to refocus scattered light to create a more uniform sheet.</p>	<p>Dalgarno <i>et al.</i> have used a SLM to correct aberrations in the light sheet through a tissue phantom [55]. The SLM also allows them to dynamically switch between two different incident beams geometries used to generate the light sheet, either a Gaussian or Bessel beam. Similarly, Schneider <i>et al.</i> have used an optimisation algorithm to create a light sheet through a turbid medium [56]. Both these examples are a nice demonstration that WFS can be used to generate more than simple foci.</p>
Endoscopic imaging	<p>Modern endoscopes are comprised of multiple flexible bundles of fibre optic cable capable of minimally invasive imaging inside the human body [57]. Each individual fibre optic cable is only capable of transmitting a single optical mode, and so many are needed to transmit an image with decent resolution. On its own, a less expensive multimode fibre acts as a turbid medium, and is unable to transmit an image instead producing a speckle pattern [11].</p>	<p>WFS can transform inexpensive multimode fibres into imaging fibres by reversing the impact of scattering along the length of the fibre.</p>	<p>A digital optical phase conjugation method was first to produce a focus through a multimode fibre [58], with the technique later being used to transfer entire images [59]. These phase conjugation methods are still reliant on measuring the scattered field for time reversal, something that would be impossible to achieve during live endoscopy. Instead, using optimisation based methods to project images through a multimode fibre may be more practical [60]. Unfortunately bending a multimode fibre causes the internal transmission matrix to shift unpredictably, rendering the previously optimised wave useless. This remains an unsolved problem.</p>

Treatment			
Photodynamic therapy	In photodynamic therapy, incident light is used to initiate a photosensitive chemical reaction that produces free radicals capable of killing biological tissue [61]. Therapeutic tumour localising photosensitizers have been developed that allow photodynamic therapy to be used as a targeted, minimally invasive method to treat cancer [62].	The scattering properties of biological targets limits photodynamic therapy to superficial depths. WFS can be used generate a deep tissue focus, triggering photosensitizers non-invasively.	The dynamic nature of biological tissue makes focus generation in deep tissue difficult [18]. Improvements in SLM speed [19] and algorithm design [25] aim to improve the speed of optimisation, such that dynamic focus generation in deep tissue is possible.
Optogenetics	Some naturally occurring ion channels are regulated by light. Optogenetics exploits either these naturally occurring, or artificially engineered [63] ion channels to study the activity of individual neurons through controllable modulation of these channels using incident light [64].	The primary advantage optogenetics has over ultrasonic neuromodulation [65] is the ability to sharply focus light such that individual nerves can be innervated. WFS can be used to achieve cell-sized focus generation through a scattering medium.	The skull provides a optical barrier that prevents optogenetic neuromodulation of neurons in the brain. Yoon <i>et al.</i> have managed to use WFS to generate an optical focus inside a mouse brain (directly through the skull), effecting a neuronal response [66]. Previous methods of transcranial optogenetics relied on an invasive fibre optic probe, which caused tissue damage.

Other			
Optical tweezing	Optical tweezers allow researchers to individually manipulate microscale particles using a highly focused laser beam - dielectric particles would become trapped in the focal point of the beam where the electric field is strongest [67].	WFS can be used to engineer large variations in the phase profile of the laser beam, which creates a stiffer optical trap [68].	Taylor <i>et al.</i> [68] have used phase-only modulation to create a stiffer optical trap that is limited by a very long optimisation time, which they later improve upon [69].
Super-resolution lenses	The maximum achievable resolution of an optical system is limited by diffraction [70]. Super-resolution imaging attempts to surpass this diffraction limit.	Using a shaped beam and a turbid medium, a focus can be generated through this “ <i>scattering super-lens</i> ” [71] with diameter below the diffraction limit of an equivalent lens system.	Both Vellekoop <i>et al.</i> [72] and Park <i>et al.</i> [71] have used scattering nanoparticles to create a turbid lens that achieves sub-diffraction limit foci. When compared with other super-resolution techniques such as metamaterial lens or near-field scanning optical microscopy the turbid lens are easier to manufacture, work at any wavelength and do not require any moving parts.

Cryptography A turbid medium can be used as a physical key for cryptography - incident light (the input) is scattered multiple times, producing a complex speckle pattern (the output). The use of optical keys are attractive as even a simple TiO₂ scatterer has sufficiently many degrees of freedom (particle number, density, size, location, refractive index, etc.) to create a practically unclonable cryptographic function [73].

Spatially modulating an incident wave can increase the complexity of the system, making it prohibitively hard to crack conventionally.

Standard turbid keys are vulnerable to emulation attacks if the challenge-response behaviour of the system is known the expected speckle pattern output can be spoofed for a given input [73]. By using two spatial light modulators and a low photon count incident beam, Gordon *et al.* have created a quantum secure authentication method [74]. The low photon count prevents characterisation of the input light [75], and as such emulation attacks are impossible [74]. Liao *et al.* have taken the opposite approach, and instead present a method of using WFS to decrypt optical keys [76]. Such methods are advantageous in that the cryptosystem doesn't have to be rigorously characterised and can instead be solved using iterative feedback based WFS methods.

Free space optical (FSO) systems are a high-bandwidth alternative to traditional radio based communication systems, and use either visible or infrared light for data transfer [77]. FSO transmitters and receivers are much cheaper than RF devices, and have fewer bandwidth constraints, however they require a direct line of sight link between transmitter and receiver, and are impaired by atmospheric turbulence [78].

A spatial light modulator would be able to control the angle of propagation of a wave from a reflecting surface, allowing a beam to effectively bend around obstacles.

Both Kaina *et al.* [79] and Najafi *et al.* [78] have proposed positioning using a SLM as the reflecting surface to control the angle of reflection of an incoming microwave or infrared wave respectively. Cao *et al.* instead suggest that an SLM can be directly built into the transmitter, which would modulate the wave to controllably reflect of the surrounding environment [80]. This method requires only a single SLM to control reflection from multiple surfaces, but remains limited by the prohibitively slow optimisation time of the SLM. This problem may be mitigated in three ways: the SLM can be better coupled to the target receiver, a faster SLM can be used (see Tzang *et al.* [19]), or stationary features in surrounding environment (walls, ceilings etc.) can be pre-scanned and shaped.

2.2 Models of Light Propagation in Tissue

2.2.1 Light Scattering by Biological Tissues

The intensity of light decreases as it propagates through biological tissue. This attenuation is caused by two mechanisms: absorption and scattering. Absorption describes how the energy of incident light decreases over distance in a specific medium, while the scattering coefficient describes how the path of light is deflected. The angle at which a photon gets deflected is known as the scattering angle. The average of the cosine of this angle across many such scattering interactions is known as the anisotropy of the material. Light propagates through this material at a set speed. The ratio of the speed of light in a vacuum to the speed of light in a given material is known as the refractive index.

2.2.2 Tissue Optical Properties

To summarise, the propagation of light through a given tissue can be characterised using four parameters:

- μ_a , the absorption coefficient, which describes the efficiency of light scattering
- μ_s , the scattering coefficient, which describes the efficiency of light absorption
- g , the anisotropy parameter, which is the average of the cosine of the angle of scattered light
- n , the real refractive index, which describes the speed of light in the medium

By controlling these four parameters, we can design realistic tissue models of scattering able to simulate wavefront shaping. Two different approaches are used: the continuum model, or the discrete particle model.

2.2.3 Continuum Model

In the continuum model of scattering the simulation domain is discretized into continuous domain of random refractive index variations. [81]. Consequently, the propagation of a incident coherent wavefront is randomly perturbed such that a random speckle pattern is generated over depth. It has been found that the spatial arrangement of these refractive index inhomogeneities can be described using the Kolmogorov model of frozen turbulence [82].

The continuum approach is well suited to modelling large, heterogeneous domains [83]. However, the size of the spatial inhomogeneities and refractive index variations have not been directly coupled to the previously mentioned tissue optical properties - instead a parameter fitting procedure is used to create the modelling domain. For example, Yang *et al.* determine the standard deviation of refractive index variation by finding the depth at which the DC and AC component of the intensity field in k-space falls to unity (this depth would represent the transport mean free path of the tissue model - an optical parameter that can be derived from the scattering coefficient and anisotropy) [6].

In this report we couple the continuum approach with the angular spectrum technique to model deep tissue scattering. We then compare two different wave shaping methods, binary amplitude and phase, using the model.

2.2.4 Discrete Particle Model

The discrete particle model instead describes tissue as a random assembly of scattering spheres (although sometimes other axisymmetric geometries are used [84, 85]). Contrary to the continuum model, the refractive index of the scatterers remains constant, instead the radius and density can be controlled to vary optical properties [83].

One major advantage of the discrete particle approach is that the modelling domain is directly coupled to tissue optical properties using analytical Mie theory

[86]. Consequently, the same principles underlying this model are frequently used to design tissue-like phantoms [87]. To more accurately capture physically realistic optical properties, it is even possible to create models where sphere radius is not fixed, but instead follows a set distribution (e.g a log-normal distribution [88]).

In this report we use the discrete particle approach to image the internal scattered field throughout a scattering medium. We show how various sphere distributions can create realistic speckle patterns, and validate the predicted optical properties of our model.

2.3 Computational Electromagnetics

2.3.1 FDTD, FEM and BEM

Having described the two approaches to modelling biological tissue we must now select an appropriate computational method for simulation. We start by considering three most common techniques [89]: the finite-difference time-domain (FDTD) method, finite element method (FEM) and the boundary element method (BEM). All three methods are rigorous: with theoretically infinite computational power all methods would be able to simulate both continuum and discrete particle models of scattering. Regrettably, we don't live in a world with unlimited computational power, and as such individual limitations make each method uniquely suitable to simulating scattering. A brief comparison of the selected methods can be found in Table 2.4.

Table 2.4: Common, rigorous, methods in computational electromagnetics.

Computational Method	Explanation	Advantages	Disadvantages
Finite-difference time-domain (FDTD)	The FDTD discretizes the computational domain in space and time into a regular grid of Yee cells, such that Maxwell's equations are reformulated into central-difference approximations that can be solved sequentially [90, 91].	The FDTD is a time domain method, and as such the solution for multiple frequencies can be solved simultaneously [92]. Further advantages include the simplicity of implementing the FDTD [93], and the manageable scaling behaviour [93]. Additionally, perfectly matched layers have been created for the FDTD method to simulate an infinite absorbing layer surrounding the computational domain [94].	The FDTD method requires a mesh density of 8-16 Yee cells per wavelength [95], and as such computational complexity grows rapidly when simulating visible light scattering through large domains. Note that the pseudospectral time-domain method uses a fast Fourier transform as opposed to finite differences to solve Maxwell's equations in space [96]. As a final note, Yee cells are cubic voxels, and as such struggle to accurately mesh curved geometries (e.g. the discrete particle model) [97].

Finite element method (FEM)	The FEM is another way to solve Maxwells equations by subdividing a complex domain in manageable, finite elements, the solution across each finite element can be solved by minimising the weighted residual error [98].	FEM allows for unstructured meshing - the domain can be irregularly divided into uniquely shaped elements (e.g. a tetrahedron or pyramid). This allows the FEM to better represent more complex geometry [99]. Furthermore, the FEM for electromagnetics has a greater potential to be coupled with other FEM physics solvers (e.g. mechanical or thermal) [93].	The FEM is predominately a frequency domain method, but can be formulated in the time domain [100]. This solution is implicit it produces a system of linear equations that must be solved (e.g. using a matrix inversion). This is more computationally taxing than the explicit solutions found in the FDTD method, but has the advantage of being unconditionally stable [99]. As a final note, mesh generation for large domains is often a surprisingly large undertaking [93].
Boundary element method (BEM)	Both the FDTD and FEM are differential methods, the BEM is an integral method meaning the integral form of Maxwells equations are solved across the surface of a computational domain [101].	As only the surface is meshed the BEM is very efficient for homogeneous domains with a low surface area to volume ratio [93].	Conversely, the BEM struggles to model complex, inhomogeneous domain, like those needed to model optical scattering.

Computational domains used to model scattering would have a very large surface area to volume ratio, and as such the BEM would be a completely unsuitable choice. We have chosen to discuss it anyway to demonstrate how a computational method which is ubiquitous in one field (radio-frequency engineering [93]), would struggle to find use in another.

The FDTD method and FEM are both more suitable choices, but both have difficulty simulating very large computational domains while maintaining an appropriate mesh width. Instead, a better computational method may be found by looking into some less general techniques.

2.3.2 The Monte-Carlo Method

The previous computational methods all use carefully designed domains - tissue optical properties are controlled through scatterer size, placement and refractive index variation. The Monte-Carlo method instead considers the bulk scattering properties of the medium, such as the scattering and absorption coefficients, and the phase function [102].

By launching photon packets into this scattering medium the path and extinction of a given photon can be determined in a probabilistic manner. For example, an incident photon travels a random distance into a turbid medium, before being absorbed (a random portion of the photon's weight is removed) and scattered (at a random angle) [103]. These steps are repeated until the photon is extinguished or exits the modelling domain. Researchers are able to simulate the scattered field inside a medium by combining the probabilistic paths of a large number of these photons.

Note that this conventional approach to photon transport using the Monte Carlo method is unable to produce a speckle image - the necessary micro-scale inhomogeneities that cause speckle are not considered. As such, the most common

implementation of the Monte Carlo method cannot be used for wavefront shaping.

However, in 2019 Bar *et al.* proposed a Monte Carlo framework capable of rendering speckle patterns using speckle statistics [104]. They are able to generate solutions much faster than competing full-wave approaches, and have demonstrated that the model can replicate optical phenomena such as the memory effect [104]. However, this method does not take a first-principles approach to speckle generation. By this we mean that microscale refractive index inhomogeneities cause scattering, which produces a speckle pattern from incident coherent light. Full wave models (e.g. FDTD, FEM) directly model these inhomogeneities and as such produce a speckle pattern. In contrast, this Monte Carlo framework characterises speckle statistically (using the mean and covariance). By not adopting a rigorous first-principles approach to speckle generation, there is a risk that the statistical formulation of speckle would become unreliable.

2.3.3 The Discrete Dipole Approximation

A scattering specific computational method that may be worth considering is the discrete dipole approximation (DDA) method. In the DDA a scattering medium is broken up into a regular array of polarisable dipoles [105]. The DDA is well suited to modelling scattering by irregular (but internally homogenous) scatterers, and has been coupled with FFT techniques leading to a significant reduction in computational time [106].

Unfortunately, like the Monte Carlo method, the DDA is poorly suited when simulating complex geometries - for example the microscale inhomogeneities used in both the discrete particle model and continuum model. The method also suffers when simulating targets with a large refractive index (> 2) [105]. Although this does not include tissue, many tissue phantom use high refractive index microspheres as scatterers [107].

2.3.4 The Angular Spectrum Method

The angular spectrum method is able to simulate the propagation of light by decomposing an incident wave field into an infinite series of plane waves using a Fourier transform [108]. These plane waves are then propagated through a given depth before an inverse Fourier transform is used to reconstruct the complex field [108]. Introducing a variation in the refractive index when propagating each plane wave results in the phase of each plane wave becoming shifted, such that over many Fourier - Inverse Fourier cycles a speckle pattern is generated [6].

This method is well suited to modelling large domains, and has been used to simulate scattering through 8mm of tissue [6]. However, similar to the Monte Carlo framework for speckle generation, the angular spectrum method does not take a first-principles approach to simulate scattering. The refractive index is randomly distributed according to a Gaussian probability function - this standard deviation is calculated by looking at the depth where photon transport becomes random relative to the initial direction. This depth is the transport mean free path of the tissue and the standard deviation is optimised to achieve a desired transport mean free path [6]. This calculated deviation is not an inherent optical property of the medium, instead it is entirely by angular spectrum specific design considerations (e.g. the number of elements for the discrete Fourier or inverse Fourier transforms, or the spacing between these transforms).

2.3.5 The T-Matrix Method

The T-Matrix method can be thought of as an expansion on standard Lorenz-Mie theory in that it allows for the calculation of a scattered field from an assembly of spherical scatterers (although other rotationally symmetrical particles can be used [85]).

By recognising that the total field is a superposition of the incident field, and the scattered field from all other scatterers in the modelling domain we are able to formulate a system of linear equations that describe scattering in a medium [109].

As the incident field can be calculated analytically, only the coefficients describing the sphere centred scattering coefficient have to be determined numerically. One downside to determining the incident beam coefficients analytically is that the arbitrarily shaped beams found in WFS are difficult to calculate - even very thin Gaussian beams are unable to be modelled [110].

The T-Matrix method is only suited to simulating discrete particle models of tissue, but nevertheless has many key advantages over competing rigorous computational techniques. Firstly, the computation is predominantly analytical, producing very accurate results [111]. Furthermore, the solution itself is only calculated on the surface of the scattering spheres (using vector spherical wave functions) leading to “*very little*” memory use and “*affordable CPU-time*” [112].

The most advantageous property of T-Matrix approaches for WFS simulation is that the elements of the T-Matrix for a given domain do not need to be recalculated for a different incident waves [111]. This would allow us to evaluate focus generation by the arbitrary incident wavefronts used for wavefront shaping dramatically faster than competing methods.

2.3.6 Requirements of a Wavefront Shaping Model

We now highlight the four most important requirements for a computational model to efficiently simulate wavefront shaping. The model:

1. **must be both time and memory efficient** - An obvious point, but if deep tissue scattering simulations are desired then many of the slower models (such as FDTD) that require sub-wavelength discretization may be a poor choice.
2. **must be a full-wave simulation that does not discard phase information** - Phase information is critical to WFS, computational methods that discard phase information (e.g. diffusion theory, that treats photon transport as a movement down concentration gradient [113]) cannot be used.
3. **must allow for arbitrary incident wavefront to be modelled** - Some meth-

ods (T-Matrix, Monte Carlo) can struggle to represent the complex shaped beams found in WFS while other methods like FDTD, FEM or the angular spectrum find the problem trivial.

4. **must take a “*first-principles*” approach to modelling a scattering domain**
 - if coherent light incident on a tissue with micro-scale refractive index inhomogeneities causes a speckle pattern, then a approach that allows us to directly model these index inhomogeneities would be most likely to capture the physics of scattering.

Unfortunately, no one method is able to meet all four requirements to an entirely satisfactory degree - instead we must prioritise what we want our model to achieve.

To this end, we propose two separate models to evaluate WFS are distinct spatial scales:

- An angular spectrum approach based on the work of Yang *et al.* [6] can be used to simulate wavefront shaping in large domains using the continuum representation of tissue. This model uses is very efficient at representing macro-scale tissue, and can naturally handle arbitrarily shaped, complex incident waves. Unfortunately, this approach characterises the scattering behaviour of tissue using an arbitrary parameter - the standard deviation of the refractive indices across a Fourier plane, and as such is not as physical as a full-wave first-principles approach.
- The T-Matrix method, specifically using the multiple sphere T-Matrix (MSTM) FORTRAN code by Mackowski [110] can be coupled with the discrete particle model of tissue to simulate scattering. This method is the most time and memory efficient full-wave approach [112]. While it is theoretically possible that this method can be expanded to represent arbitrary incident beams [114], in the meantime it is possible to decompose any complex shaped wavefront into a series of solvable plane waves using the angular spectrum approach [108].

These two models can be best applied by considering the desired research goal beforehand. For example, the angular spectrum model can be used to evaluate different wavefront shaping algorithms, or may be used as Yang *et al.* have to investigate the impact different factors such as noise or SLM geometry have on focus generation. The T-Matrix approach would be better suited to studying the internal field of a scattering medium, and any other poorly understood phenomena such as the memory effect.

Chapter 3

Methods

3.1 The Two Models

We have identified two distinct, but useful scattering models and will now briefly explain how we plan to use each in this thesis.

We propose that the angular spectrum approach will be best suited to either investigate the impact of confounding factors on wavefront shaping (e.g. noise or guidestar size [6]), or to evaluate various optimisation algorithms or wave shaping approaches.

Current techniques for comparing various optimisation algorithms use entirely non-physical random transmission matrices to simulate scattering [20]. This method is satisfactory for comparing the algorithms found in Table 2.2, but more modern approaches leverage machine learning to decrease optimisation time [115, 116]. These recent machine learning algorithms look at patterns within the developing speckle to speed up focus generation, and as such cannot be evaluated using simple random transmission matrix based approaches. Instead the angular spectrum method may be used to generate more physical deep tissue speckle patterns that can assist the development of these machine learning based algorithms.

Similarly, no one has investigated the difference between the theoretical WFS

enhancement factors (see Table 2.1) and the experimental results which can be as great as 30% [11]. Are these differences really caused by temperature fluctuations or mechanical vibration [11]? An angular spectrum model comparing the enhancement produced by a phase based or amplitude based spatial modulation may be useful.

In this report we begin to formulate the answers to these questions by using the angular spectrum method to simulate iterative focus generation using the stepwise-sequential algorithm [4] to create a binary amplitude and binary phase shaped focus through $8mm$ of scattering tissue.

On the other hand, the T-Matrix method is well suited to look inside a physically realistic scattering medium. Investigations of the memory effect [5] and feedback based WFS [5] have all been performed experimentally and as such are limited by the usual experimental constraints (cannot see inside the medium, incomplete control over medium parameters, effect of noise, etc.). We propose that many of the questions found in Section 1.2 (that won't be restated for brevity) can be answered using a T-Matrix based simulation approach.

To this end, we show that the T-Matrix method can generate physically realistic speckle patterns, and can be used to visualise the internal field of a turbid medium. We also demonstrate that the T-Matrix method can be directly used to simulate tissue-like media with the discrete particle model by comparing the scattering coefficient and anisotropy determined using the T-Matrix method against the values calculated using analytical Mie theory and the inverse adding-doubling method [117].

3.2 Mathematical Theory

We proceed by formulating the mathematical theory underlying the two models.

3.2.1 The Angular Spectrum Method

The angular spectrum method is (by far) the simplest model. In this method an arbitrarily complex incident wave, $E_s(x, y)$, is decomposed into an infinite series of plane waves using a 2D Fourier transform [6]:

$$\hat{E}_S(k_x, k_y) = \frac{1}{2\pi} \int \int E_s(x, y) \exp[-i(k_x x + k_y y)] dx dy \quad (3.1)$$

where \hat{E}_S is now the amplitude of the complex plane wave and k_x and k_y are the spatial frequencies in the x and y direction respectively [6], We now propagate these plane wave forward in space a given distance, d :

$$\hat{E}_D(k_x, k_y) = \hat{E}_S(k_x, k_y) \exp \left[i \cdot n \cdot d \cdot \sqrt{\left(\frac{2\pi}{\lambda}\right)^2 - k_x^2 - k_y^2} \right] \quad (3.2)$$

Where \hat{E}_D is the propagated plane wave, and n the refractive index. Finally, by performing an inverse Fourier transform we are able to reconstruct across this depth:

$$E_D(x, y) = \frac{1}{2\pi} \int \int \hat{E}_D(k_x, k_y) \exp[i(k_x x + k_y y)] dk_x dk_y \quad (3.3)$$

Computationally, the above procedure is performed using a fast Fourier transform (FFT) and inverse Fourier transform (iFFT) within MATLAB. In the Yang *et al.* implementation of the angular spectrum model on each element of the FFT-iFFT propagation matrix the refractive index is varied according to a Gaussian random distribution:

$$(x) = \frac{1}{n_\sigma \sqrt{2\pi}} e^{-\frac{1}{2} \left(\frac{x-n_\mu}{n_\sigma}\right)^2} \quad (3.4)$$

Where n_μ is the refractive index mean and n_σ is the refractive index standard deviation that control the scattering behaviour of the method. By repeating these FFT-iFFT steps the propagation of light into a deep tissue medium can be simulated.

3.2.2 The T-Matrix Method

As a preliminary warning, note that most of the mathematical formalisation found in this section is taken from the work of T-Matrix pioneers Mackowski and Mishchenko [118]. Much to this author's chagrin, there appears to be no concise way to mathematically describe the T-Matrix method. Instead, a choice must be made on where to truncate the explanation to prevent leading the reader down long tangents about the vector spherical wave function translation rule, or Wigner d-functions. A much more comprehensive explanation of the T-Matrix method can be found in this textbook by Mishchenko *et al.*[119], or for an explanation of how this method is implemented computationally see this paper also by Mackowski and Mishchenko [110]. Ultimately, in this section we hope that the reader can leave understanding what the T-Matrix is, and what coefficients must be solved to reach a solution.

We use the T-Matrix method to calculate the field scattered by an assembly of independent spheres. The total scattered wavefront, E_{total} , would be a linear combination of the scattered field (E_{sca}) from each sphere, i , and the incident field (E_{inc}) [119]:

$$\mathbf{E}_{total} = \mathbf{E}_{inc} + \sum_{i=1}^{N_s} \mathbf{E}_{sca}^i \quad (3.5)$$

To calculate the scattered field from each sphere we must know what light is incident on that sphere - logically this would be a combination of the incident field and the scattered light from every other sphere in the model. Therefore we begin by calculating the vector spherical wave function (VSWF) expansions of the incident and scattered field centred around the origin of i -th sphere in the cluster:

$$\begin{aligned} \mathbf{E}_{scat}^i &= \sum_{n=1}^{\infty} \sum_{m=-n}^n [a_{mn}^i \mathbf{M}_{mn}^3(Kr^i, \theta^i, \phi^i) + b_{mn}^i \mathbf{N}_{mn}^3(Kr^i, \theta^i, \phi^i)] \\ \mathbf{E}_{inc}^i &= \sum_{n=1}^{\infty} \sum_{m=-n}^n [p_{mn}^i \mathbf{M}_{mn}^1(Kr^i, \theta^i, \phi^i) + q_{mn}^i \mathbf{N}_{mn}^1(Kr^i, \theta^i, \phi^i)] \end{aligned} \quad (3.6)$$

Where K is the wavenumber, r, θ, φ are the radius, polar angle and azimuthal angle respectively, m is the degree and n the order of the VSWFs, a_{mn}, b_{mn}, p_{mn} and q_{mn} are the unknown coefficients. M_{mn}^1 and N_{mn}^1 are regular VSWFs, while M_{mn}^3 and N_{mn}^3 are radiating VSWFs. VSWF are functions that are solutions to the Helmholtz equation constructed from regular Bessel functions, the distinction between regular and radiating VSWFs are important as only radiating VSWFs are formulated with the Hankel function which ends up satisfying the Sommerfeld radiation condition [120].

To calculate the light incident on the i -th sphere we must rewrite the scattered field VSWF expansion about each sphere for all other spheres. To do so we use the addition theorem for VSWFs [118]:

$$\begin{aligned} \mathbf{M}_{mn}^3(Kr^i, \theta^i, \varphi^i) &= \sum_{l=1}^{\infty} \sum_{k=-l}^l [A_{mnkl}^{(3)}(KR^{ij}, \Theta^{ij}, \Phi^{ij}) \mathbf{M}_{kl}^1(Kr^i, \theta^i, \varphi^i) \\ &+ B_{mnkl}^{(3)}(KR^{ij}, \Theta^{ij}, \Phi^{ij}) \mathbf{N}_{kl}^1(Kr^i, \theta^i, \varphi^i)] \end{aligned} \quad (3.7)$$

$$\begin{aligned} \mathbf{N}_{mn}^3(Kr^i, \theta^i, \varphi^i) &= \sum_{l=1}^{\infty} \sum_{k=-l}^l [A_{mnkl}^{(3)}(KR^{ij}, \Theta^{ij}, \Phi^{ij}) \mathbf{N}_{kl}^1(Kr^i, \theta^i, \varphi^i) \\ &+ B_{mnkl}^{(3)}(KR^{ij}, \Theta^{ij}, \Phi^{ij}) \mathbf{M}_{kl}^1(Kr^i, \theta^i, \varphi^i)] \end{aligned} \quad (3.8)$$

Where R^{ij}, Θ^{ij} , and Φ^{ij} is the distance, polar angle, and azimuthal angle between spheres i and j , and k and l are the degree and order of the new expansions. Note that unlike the previous expansion coefficients, $A_{mnkl}^{(3)}(KR^{ij}, \Theta^{ij}, \Phi^{ij})$ and $B_{mnkl}^{(3)}(KR^{ij}, \Theta^{ij}, \Phi^{ij})$ are entirely dependent on the locations of sphere i and j and do not have to be calculated.

It is now possible to use Equations 3.7 and 3.8 to create a linear relationship

between the scattering coefficients and incident coefficients:

$$a_{mn}^i = \bar{a}_n^i \left[p_{mn}^i - \sum_{\substack{j=1 \\ j \neq i}}^{N_s} \sum_{l=1}^{L_s} \sum_{k=-l}^l [A_{klmn}^{(3)}(KR^{ij}, \Theta^{ij}, \Phi^{ij}) a_{kl}^j] \right. \\ \left. + B_{klmn}^{(3)}(KR^{ij}, \Theta^{ij}, \Phi^{ij}) b_{kl} * j \right] \quad (3.9)$$

$$b_{mn}^i = \bar{b}_n^i \left[p_{mn}^i - \sum_{\substack{j=1 \\ j \neq i}}^{N_s} \sum_{l=1}^{L_s} \sum_{k=-l}^l [A_{klmn}^{(3)}(KR^{ij}, \Theta^{ij}, \Phi^{ij}) b_{kl}^j] \right. \\ \left. + B_{klmn}^{(3)}(KR^{ij}, \Theta^{ij}, \Phi^{ij}) a_{kl} * j \right] \quad (3.10)$$

where L_s is the truncation order of the VSWF expansion and \bar{a}_n^i and \bar{b}_n^i are the same coefficients found in Lorenz/Mie theory [86]:

$$\bar{a}_n^i = \frac{m^i \psi_n'(x^i) \psi_n(m^i x^i) - \psi_n(x^i) \psi_n'(m^i x^i)}{m_i \xi_n'(x^i) \psi_n(m^i x^i) - \xi_n(x_i) \psi_n'(m^i x^i)} \\ \bar{b}_n^i = \frac{\psi_n'(x^i) \psi_n(m^i x^i) - m^i \psi_n(x^i) \psi_n'(m^i x^i)}{\xi_n'(x^i) \psi_n(m^i x^i) - m^i \xi_n(x_i) \psi_n'(m^i x^i)} \quad (3.11)$$

where x is the size parameter of the i -th sphere and ψ_n and ξ are Ricatti-Bessel functions [118].

Before proceeding with formulating the T-Matrix consider the incident expansion coefficient - p_{mn}^i and q_{mn}^i . They can actually be determined analytically. For a incident plane wave propagating towards the shared target origin at azimuthal angle α and polar angle β this becomes:

$$\begin{pmatrix} p_{mn}^i \\ q_{mn}^i \end{pmatrix} = -4\pi i^{n+1} e^{-im\alpha} \begin{pmatrix} \tau_{mnp}(\cos \beta) \\ i\tau_{mn(3-p)}(\cos \beta) \end{pmatrix} \quad (3.12)$$

where $\tau_{mn(3-p)}$ is:

$$\tau(\cos \beta) = -\frac{1}{4} \left(\frac{2n+1}{\pi} \right)^{1/2} \left((-1)^p \mathcal{D}_{-1m}^{(n)}(\cos \beta) + \mathcal{D}_{1m}^{(n)}(\cos \beta) \right) \quad (3.13)$$

with \mathcal{D} being the Wigner d-function [119]. Incident Gaussian beams can also be represented as a VSWF expansion using the localized approximation [121]:

$$\begin{pmatrix} p_{GB,mn} \\ q_{GB,mn} \end{pmatrix} = \bar{g}_n \begin{pmatrix} a_{PW,mn} \\ b_{PW,mn} \end{pmatrix} \quad (3.14)$$

Where \hat{s} is the polarisation state and \bar{g}_n is:

$$\bar{g}_n = \exp\left(\frac{n+1/2}{k\omega_0}\right)^2 \quad (3.15)$$

and ω_0 is the Gaussian beam width at the focus. Note that this approximation only holds when $K\omega_0 \geq 5$ [121]. Ultimately, for both incident waves, this means that the only unknown coefficients are a_{mn}^i and b_{mn}^i . It is convenient to create a compact form of Equations 3.9 and 3.10 which contain these unknowns:

$$\mathbf{a}_{mnp}^i + \bar{\mathbf{a}}_{np}^i \sum_{\substack{j=1 \\ j \neq i}}^{N_s} \sum_{l=1}^{L_s} \sum_{k=-l}^l \sum_{q=1}^2 H_{mnpklq}^{ij} \mathbf{a}_{klq}^j = \bar{\mathbf{a}}_{np}^i \mathbf{p}_{mnp}^i \quad (3.16)$$

With the subscripts p and q representing the TM and TE modes and have the values of 1 or 2 respectively. H is also used as shorthand to represent the Hankel function addition coefficient, A and B :

$$\begin{aligned} H_{mn1kl1}^{ij} &= H_{mn2kl2}^{ij} = A_{klmn}^{(3)}(kR^{ij}, \Theta^{ij}, \Phi^{ij}) \\ H_{mn1kl2}^{ij} &= H_{mn2kl1}^{ij} = B_{klmn}^{(3)}(kR^{ij}, \Theta^{ij}, \Phi^{ij}) \end{aligned} \quad (3.17)$$

Inverting Equation 3.16 now allows us to identify the eponymous T-Matrix:

$$\mathbf{a}_{mnp}^i = \sum_{j=1}^{N_s} \sum_{l=1}^{L_s} \sum_{k=-l}^l \sum_{q=1}^2 T_{mnpklq}^{ij} \mathbf{p}_{klq}^j \quad (3.18)$$

This T-Matrix is the only aspect of the method that is determined numerically. Within the software package MSTM (which was used for this report) the T-Matrix is solved using the bi-conjugate gradient method [110]. Having determined the scattering expansion coefficients the field can be found from Equations 3.5 and 3.6.

3.3 Generating the Model Domain

Both models are unique in representing a scattering medium. The angular spectrum approach uses a variant of the continuum method, by which a turbid medium is modelled as normally distributed refractive index variations across a series of FFT-iFFT planes. In contrast, the T-Matrix method is explicitly a discrete particle based approach - scatterer geometry, location and refractive indices define the scattering response of the medium. The methods of generating these distinct modelling domains are described below.

3.3.1 Angular Spectrum and the Continuum Model

Yang *et al.* define the depth between FFT-iFFT pairs to be $20\mu m$, with the only requirement being that this length was significantly smaller than the transport mean free path length of the medium [6]. To simulate the desired $8mm$ of tissue means that 400 angular spectrum pairs are needed. Each FFT-iFFT plane is discretized into 2048×2048 points with a spacing of $5\mu m$. Using these measurements we can calculate the geometry of the entire modelling domain, which is a rectangular cuboid of dimensions $10.24mm \times 10.24mm \times 8.00mm$.

We continue by defining the SLM geometry - we spatially modulate the wave by applying a phase or amplitude mask of size 64×64 on the incident beam, such that each SLM element simultaneously modulates 32×32 elements of the FFT-iFFT plane.

The parameter $n_\mu = 1.4$ as this refractive index is approximately the value of biological tissue [6], while the value of n_σ was determined by parameter fitting. By looking in k-space for the depth at which the DC component (representing ballistic light) and average AC component (scattered light) of intensity become equal should give you the transport mean free path length of the model. As such $n_\sigma = 1.6 \times 10^{-1}$ to produce a mean free path length of $1mm$, matching tissue [6].

This is a very tenuous way to characterise the optical properties of biological tissue.

It is difficult to quantify exactly at what distance the DC and AC components fall to unity, and even a small fluctuation in n_σ dramatically changes the transport mean free path length. Secondly, the transport mean free path, l' , is defined as:

$$l' = \frac{1}{\mu_a + \mu_s(1 - g)} \quad (3.19)$$

By just using the transport mean free path to characterise tissue no distinction is made between the absorption coefficient, the scattering coefficient or the anisotropy as all are included in the definition. For example, a highly absorbing by lowly scattering material may have the exact same l' as a lowly absorbing but highly scattering material and as such it is impossible to say the medium used representative of biological tissue.

A consequence of not using an correct tissue optical properties in this method is that the chosen value of n_σ is entirely dependent on the geometry of our simulation (e.g. the distance between scattering planes, or element width) [6].

Despite being unable to realistically characterise tissue, the angular spectrum method can be used to provide a more realistic framework (compared to the simple matrix based approach) to evaluate different optimisation algorithms and shaping methods.

3.3.2 T-Matrix and the Discrete Particle Model

The T-Matrix method is exclusively a discrete particle based method, and as such to define the model we must specify: the number of spheres and the position, radius and refractive index of each sphere [110]. Sphere boundaries are not able to intersect, but multi-layered spheres can be created.

3.3.2.1 Domain Generation

To generate this multisphere domain we create a MATLAB code to randomly place spheres within a confining geometry. The input parameters for this code are:

- N_s - the number of spheres

- ρ_s - the sphere density (as volume fraction)
- r_s - the radius of the spheres
- n_s - the complex refractive index of the spheres
- n_b - the complex refractive index of the background

The code starts by determining the total simulation domain size:

$$V_{total} = \frac{4}{3}\pi r_s^3 \times N_s \times \frac{1}{\rho_s} \quad (3.20)$$

We then define a constraining geometry with volume V_{total} into which N_s spheres can be randomly placed. For shapes which have only one parameter defining the volume (e.g. a cube with edge length, or a sphere with radius) the constraining domain can be automatically defined. However, more complex geometries require the sizes to either be constrained or explicitly defined (e.g. to create a cylinder of volume V_{total} either the radius or height must be defined).

The code then iterates across, placing a sphere randomly within this confining geometry and checks for any intersecting surfaces. The code repeats until N_s non-intersecting spheres have been placed.

This method struggles to place all spheres at higher densities, instead the Lubachevsky-Stillinger algorithm may be applied to achieve higher sphere packing [122]. It would be unlikely to need this however, as most discrete particle models use a low density [88].

Finally, the code also allows for a radius distribution to be defined rather than a fixed radius for each sphere. Discrete particle models that use a radius distribution are better able to model both the scattering coefficient and anisotropy of biological tissue [88], a important point that will be discussed more later.

3.3.2.2 Determining the Domain Parameters

Lorenz-Mie theory is used to determine the correct particle density to produce a modelling domain with a specific scattering coefficient and anisotropy from spheres of a set radius and refractive index. The Lorenz-Mie theory is a well known analytical solution that describes how a sphere scatters an incident plane wave [86]. Practically, we use it in the following manner to create our discrete particle domain:

1. *Choose a scatterer* - Rutile titanium dioxide is a sensible choice due to the high refractive index causing stronger scattering for a given number of spheres. We find the diameter of rutile TiO₂ to be $\approx 1\mu m$ and the refractive index to be 2.5836 at a wavelength of 633nm [123].
2. *Choose a target scattering coefficient or anisotropy* - Lets say we want a tissue equivalent $\mu_s \approx 100cm^{-1}$ [124].
3. *Use a Lorenz-Mie solver to find the density that gives you the desired scattering coefficient* - We use MATLAB code provided by Bohren and Huffman modified by us to calculate the scattering coefficient and anisotropy at multiple wavelengths [125].

In the above example we find that a density of 0.25% produces a scattering coefficient around $100cm^{-1}$ (see Figure 3.1). Note that although this scattering coefficient is realistic for biological tissue, the anisotropy is not (tissue is predominately forward scattering, with $g = [0.7 - 0.9]$ [2]). This is a limitation of using only one scatterer radius to describe tissue optical properties, and will be discussed more later.

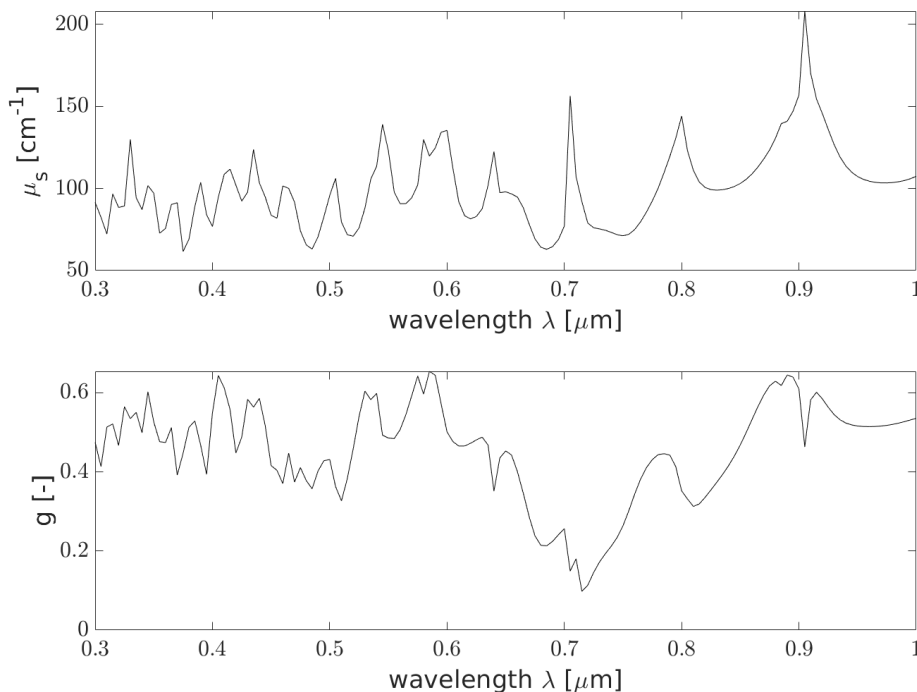


Figure 3.1: Using the Lorenz-Mie theory to determine the scattering coefficient (μ_s) and anisotropy (g) of a multisphere domain where density = 0.25%, sphere diameter = $1\mu m$ and the refractive index = 2.5836 (the diameter and refractive index of rutile TiO₂). We can use Lorenz-Mie theory as a simple way to design discrete particle models for use in T-Matrix simulations.

3.4 Scaling within MSTM

As previously mentioned, the T-Matrix simulations in this report we performed using the MSTM FORTRAN code created by Mackowski [110]. The code has been parallelised with a distributed memory architecture using the Message Passing Interface (MPI) standard [110]. In distributed memory systems each thread is allocated its own private memory, which is useful when running software over computer clusters [126]. However, this method of parallelisation causes problems when running MSTM with multiple cores on a single computer. As each core is allocated memory independently, the memory requirements quickly grow unfeasibly large for more difficult simulations [127].

Other researchers using MSTM have coped with this limitation by constraining the

number of cores used for larger runs [127], although this obviously has a significant impact on computational time. Our solution was to partially parallelise MSTM using a shared memory architecture - specifically the Open Multi-Processing standard (OpenMP). Shared memory systems, as the name suggests, creates a shared memory pool that can be accessed by each thread [126].

At present, we have used OpenMP to parallelise the near field calculation within MSTM - Equation 3.5 is evaluated in parallel at multiple locations to construct an entire near field plane. Recall that T-Matrix methods only have to calculate the T-Matrix once for a given domain, we can then calculate the near field repeatedly for different incident wavefronts using our memory efficient parallelization.

To investigate the scaling behaviour of our hybrid OpenMP-MPI version of MSTM we generate multiple sphere clusters with a variable total sphere count using the methods described in 3.3.2.1, where we set $\rho_s = 0.01$, $r_s = 0.5\mu m$, $n_s = 2.5836 + 0i$ and $n_b = 1 + 0i$. We then use the package Dstat [128] to investigate the effect the scaling behaviour of MSTM with respect to clock time and memory usage.

3.5 Validation

3.5.1 Diffraction Patterns with the Angular Spectrum Method

To evaluate our implementation of the Yang *et al.* angular spectrum approach we use our MATLAB code to simulate the Fresnel diffraction pattern of a plane wave passing through a circular aperture, then compare the result against another existing numerical solution [129].

Specifically, we simulate Fresnel diffraction of light with a wavelength of $\lambda = 633nm$ through a circular aperture of radius $1mm$ that propagates $1m$ through a vacuum. We compare our results against another numerical method for simulating Fresnel diffraction patterns - the two-step propagation method. To generate this ground-truth we use code based on a MATLAB script written by Schmidt [130].

3.5.2 Single Sphere Simulation

To validate MSTM and ensure we are using the software properly we simulate the scattering of a plane wave incident on a single sphere of diameter $1\mu m$. We then compare this result against an analytical solution provided by a Lorenz-Mie theory solver (code provided by my supervisor - Dr Munro).

In both simulations we set the wavelength $\lambda = 633nm$ and the sphere refractive index $n_s = 2.5836$. We truncate the infinite Mie series at an order of 100, to determine if this is large enough we can apply the Wiscombe criterion to determine the minimum truncation order L_0 needed:

$$L_0 = x + 4.05x^{1/3} + 2 \quad (3.21)$$

where x is the particle size parameter, $x = \frac{2\pi r}{\lambda}$. For our sphere size and wavelength we find $N_0 \approx 9$, so our value of 100 is more than enough.

3.5.3 Scattering Simulations in MSTM

If we wish to eventually use the T-Matrix method to study wavefront shaping then we must have complete confidence that MSTM is able to correctly model whatever domain we wish to simulate. To this end, we compare we wish to compare MSTM derived optical properties (μ_s, g) against both the theoretical values from Lorenz-Mie theory, and the estimated μ_s and g from Inverse Adding Doubling (IAD) [117].

IAD is a method that can determine the μ_a, μ_s and g of a scattering medium by propagating light into a disk-shaped sample of that medium with thickness δ and making three measurements:

1. *the reflectance, M_R* - which is a measure of the amount of light reflected by a scattering medium normalised by the incident light.
2. *the transmittance, M_T* - which is a measure of the amount of light that passes through a scattering medium normalised by the light that would have passed had the medium not existed.

3. *the unscattered transmittance, M_U* - which is a measure of the amount of light that passes through a scattering medium without being scattered, normalised by the light that would have passed without the medium.

IAD is commonly used to characterise the optical properties of a sample [131]. Experimentally, measurements of M_R and M_T are done using integrating spheres placed either before or after the sample [117], although we can make the same measurements experimentally by recording the total light intensity on a plane directly before or behind our simulated scattering medium (see Figure 3.2).

Measuring M_U is often done by placing a detector some distance away from the scattering medium directly in the path of the Gaussian beam. A aperture is used to spatially filter the scattered light, such that only the unscattered light is detected. To replicate this spatial filtering using our model we make multiple measurements of the ballistic light at multiple distances from the scattering medium, averaging these values together results in the intensity of only the unscattered light.

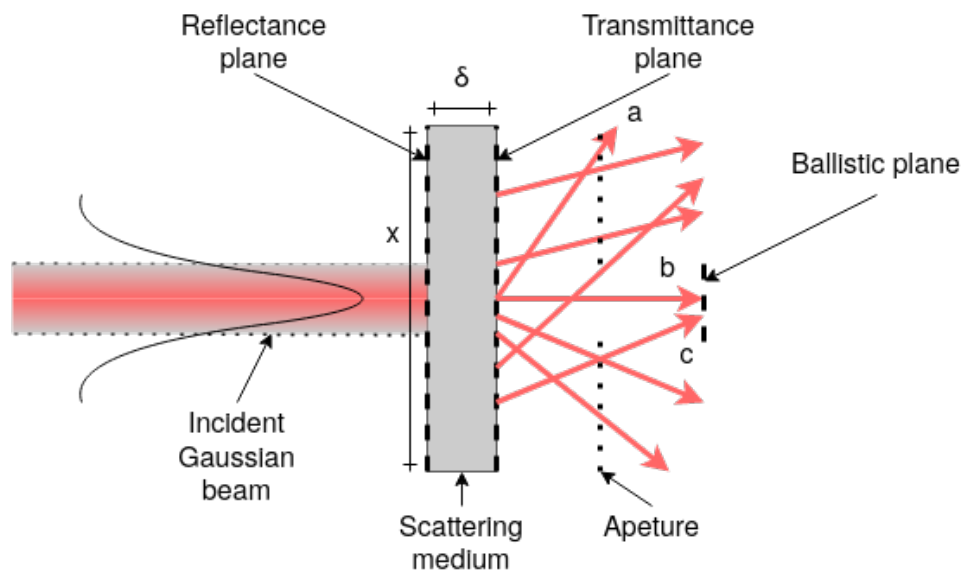


Figure 3.2: In Inverse Adding Doubling (IAD) measurements the reflectance, transmittance and ballistic light can be used to calculate the optical properties of a scattering medium. Using the T-Matrix method we simulate the scattering of an incident Gaussian beam and record reflectance and transmittance by evaluating the near field intensity directly on the planes shown. To measure ballistic light we average the measured intensity at multiple distances behind the scatterer to simulate the effect of spatial filtering using an aperture.

Note from Figure 3.2 that any light that escapes from the sides of the medium would not be detected by either the reflectance or transmittance planes. This is an experiential and computational limitation of IAD that can be minimised through appropriate design of the scattering medium.

By minimising the size of the incident Gaussian beam, and maximising the diameter of the scattering medium, we can reduce the amount of light escaping from the sides of the medium. To this end we impose a size constraint on the domain: the radius must be $\times 2$ the thickness, δ . We also define the width of the incident Gaussian beam to be 1/10th the domain radius to further minimise light escaping from the sides.

3.6 Speckle Generation with the T-Matrix

We end by plotting the speckle patterns that are generated using the T-Matrix method. We use the same size constrain defined in the previous section to generate scattering disks with a variable number of spheres, propagate a plane wave ($\lambda = 633nm$) through them and evaluate the speckle statistics of the generated speckle patterns.

Chapter 4

Results

4.1 The Angular Spectrum Method

4.1.1 Diffraction Patterns

To validate our implementation of the Yang *et al.* angular spectrum approach to simulate scattering we use our code to simulate the Fresnel diffraction of a plane wave through a circular aperture and compare our result against the two-step solution found in Schmidt [130].

Specifically, we simulate the diffraction of light with wavelength $\lambda = 633nm$ through an aperture of $1\mu m$ radius that propagates a distance of $1m$ through a vacuum. Our diffraction patterns can be found in Figure 4.1.

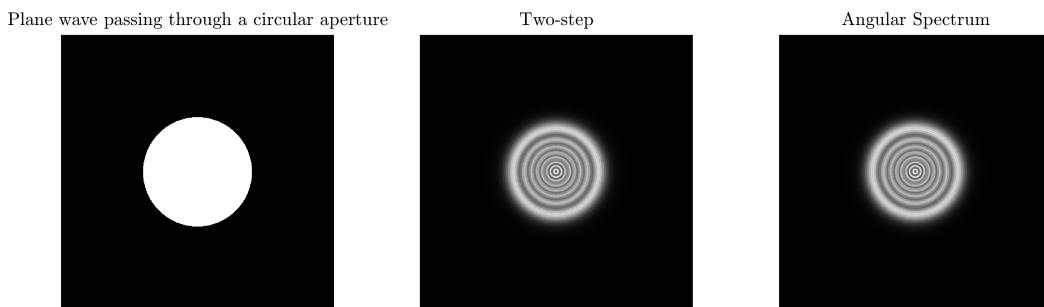


Figure 4.1: The Fresnel diffraction pattern of a plane wave with wavelength $\lambda = 633nm$ passing through an aperture of $1\mu m$ radius after propagating $1m$. We compare our angular spectrum based solution against a two-step solution found in Schmidt [130] and find the two identical.

Alternatively, it is possible to simulate the propagation of a plane wave that is obstructed by a circular aperture of the same size. Doing so allows us to observe the formation of an Arago spot (see Figure 4.2)

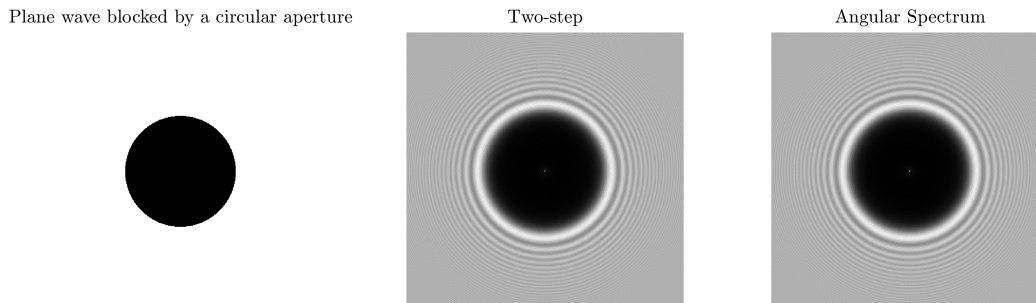


Figure 4.2: The Fresnel diffraction pattern of a plane wave with wavelength $\lambda = 633nm$ obstructed by an aperture of $1\mu m$ radius after propagating $1m$. Like Figure 4.1, we compare our angular spectrum based solution against a two-step solution found in Schmidt [130] and find the two identical. Look closely to notice the presence of an Arago spot at the centre of the circular shadows.

4.1.2 Binary Amplitude and Phase Modulation

We base our WFS angular spectrum simulation on the model proposed by Yang *et al.*, who define the distance between FFT-iFFT pairs to be $20\mu m$ [6]. To simulate the desired $8mm$ of tissue means that 400 angular spectrum pairs are needed. Each FFT-iFFT plane is discretized into 2048×2048 points with a spacing of $5\mu m$. Using these measurements we can calculate the geometry of the entire modelling domain, which is a rectangular cuboid of dimensions $10.24mm \times 10.24mm \times 8.00mm$. Through this domain, we simulate the propagation of a flat-top circular aperture beam of width $10mm$. We spatially modulate this wave by applying a phase or amplitude mask of 64×64 elements on the incident beam, such that each SLM element simultaneously modulates 32×32 elements of the FFT-iFFT plane.

We used a stepwise sequential algorithm that either modulated phase or amplitude to generate a focus. Recall from Table 2.2 that this algorithm is by far the slowest approach, but is guaranteed to find the optimal focus as every permutation for each element is tested sequentially. We generate our focus inside a $1mm$ diameter spot at the centre of the imaging plane.

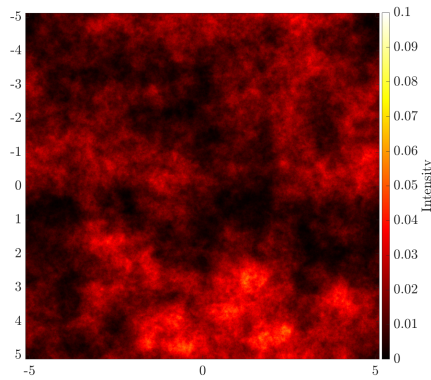


Figure 4.3: Scattered field through 8mm of tissue prior to any wavefront modulation that has been calculated using the angular spectrum method. Note how light intensity is uniformly low.

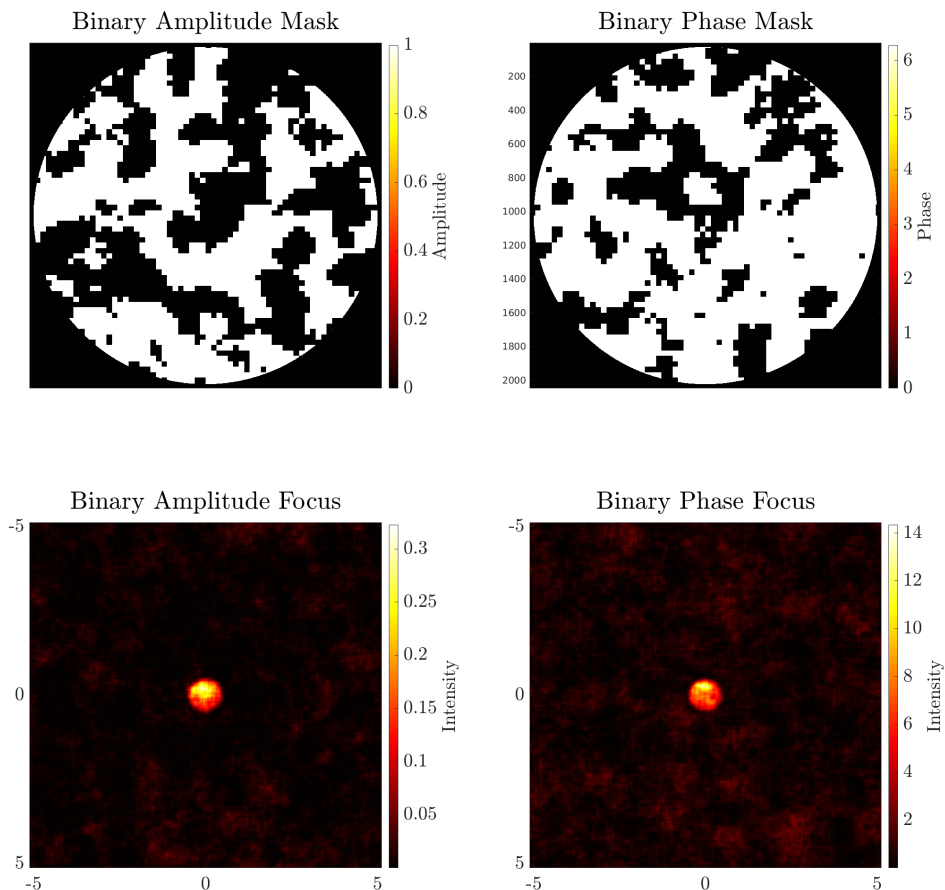


Figure 4.4: Top row: binary amplitude and phase masks determined via the angular spectrum method. These maps can be used to spatially modulate the incident beam to produce the focuses found on the bottom row. Note the difference in intensity for the amplitude and phase modulation simulations - binary phase modulation produces a brighter focus, but the background is also much brighter.

Figure 4.3 shows us the scattered field before any attempt at wavefront shaping, the light intensity is low across the entire imaging plane. As mentioned, the stepwise sequential algorithm was used to produce the binary amplitude and phase focuses found in Figure 4.4. Optimisation time took approximately 6 hours on Intel Xeon Gold 6148 CPU.

We calculate the focus enhancement, η , by measuring the mean intensity inside the focus, I_{focus} , normalised by the mean intensity before any wavefront shaping, I_{before} [14]:

$$\eta = \frac{I_{\text{focus}}}{I_{\text{before}}} \quad (4.1)$$

We also calculate the predicted enhancement, η_{pred} , from Equation 2.1 and the peak to background ratio of our generated focus, η_{PBR} , which we define as the mean intensity inside the focus, I_{focus} , normalised by the background intensity, $I_{\text{background}}$

$$\eta_{\text{PBR}} = \frac{I_{\text{focus}}}{I_{\text{background}}} \quad (4.2)$$

the results for both can be found below in Table 4.1:

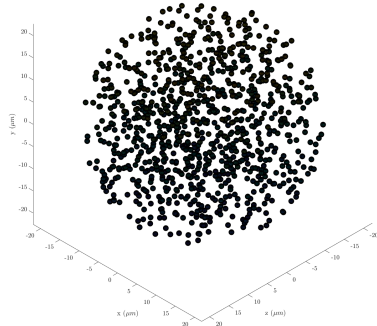
Table 4.1: Focus enhancement for binary amplitude or phase modulation simulated using the angular spectrum method.

Modulation	η	η_{pred}	η_{PBR}
Binary amplitude	10.54	652	22.85
Binary phase	410.9	1304	11.89

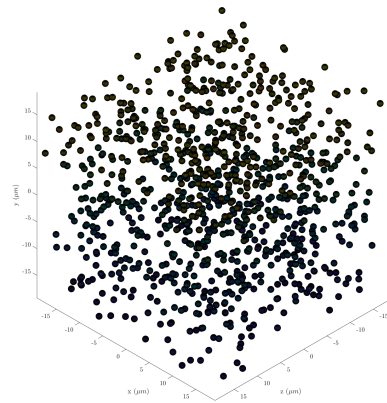
4.2 The T-Matrix Method

4.2.1 Generating Discrete Particle Models

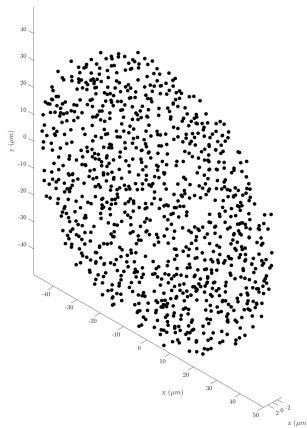
Using the methods described in Section 3.3.2 we are able to use our MATLAB code to generate various discrete particle models of scattering tissue for use in MSTM. Both the confining geometry, density, and radius distribution of these multi-sphere domains can be controlled, as shown in Figure 4.5.



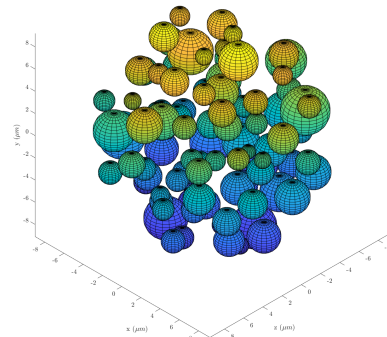
(a) 1000 spheres of diameter $1\mu\text{m}$ and density 1% constrained automatically with a bounding sphere.



(b) 1000 spheres of diameter $1\mu\text{m}$ and density 1% constrained automatically with a bounding cube



(c) 1000 spheres in a using a cylindrical constraint. In this case we specify that the radius has to be double the thickness of the disk.

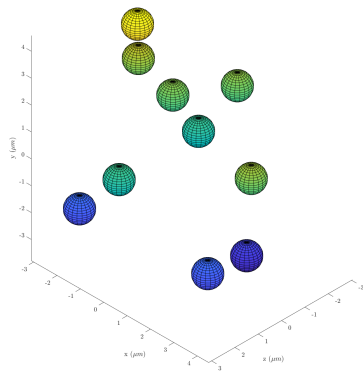


(d) A distribution can be used to define the radii of the spheres. In this case, a log-normal distribution create a 100 sphere domain with a density of 10%.

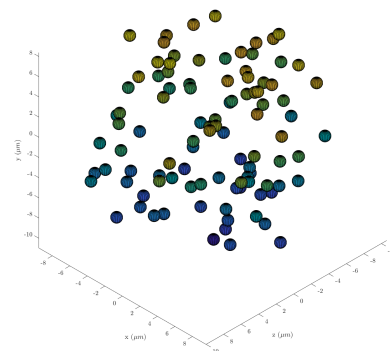
Figure 4.5: Using the method described in Section 3.3.2 we have created code that can generate discrete particle models for scattering calculations. The sphere radius, density, refractive index, total sphere count and constraining geometry can all be specified. Different distributions can be used to define sphere radii if desired.

4.2.2 Scaling with MSTM

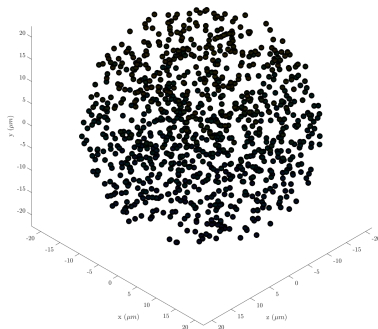
We generate multiple scattering domains up to and including 10,000 spheres using a fixed particle size of $r_s = 1\mu m$, $\rho_s = 0.25\%$ and $n_s = 2.5836$ (see Figure 4.6). We then use MSTM to simulate the scattering of an incident plane wave, using Dstat to measure time taken and memory usage. We run MSTM in parallel over four cores with a Intel Xeon Gold 6148 CPU on a system with 128 GB of RAM.



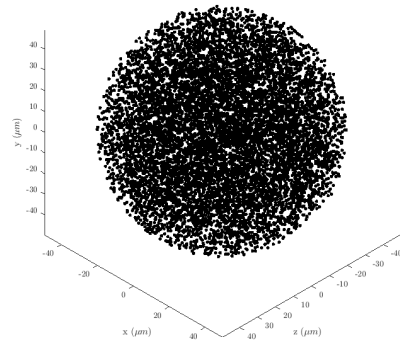
(a) 10 spheres.



(b) 100 spheres.



(c) 1000 spheres.



(d) 10000 spheres.

Figure 4.6: We create many sized multi-sphere domains upto 10000 spheres to investigate scaling using the T-Matrix method.

We plot clock time as a function of sphere number in Figure 4.7. We then use polynomial regression to determine a criterion for estimating simulation time as a function of sphere count:

$$\text{simulation time} = 1.53 \times 10^{-6} \times \text{sphere count}^{2.81} \quad (4.3)$$

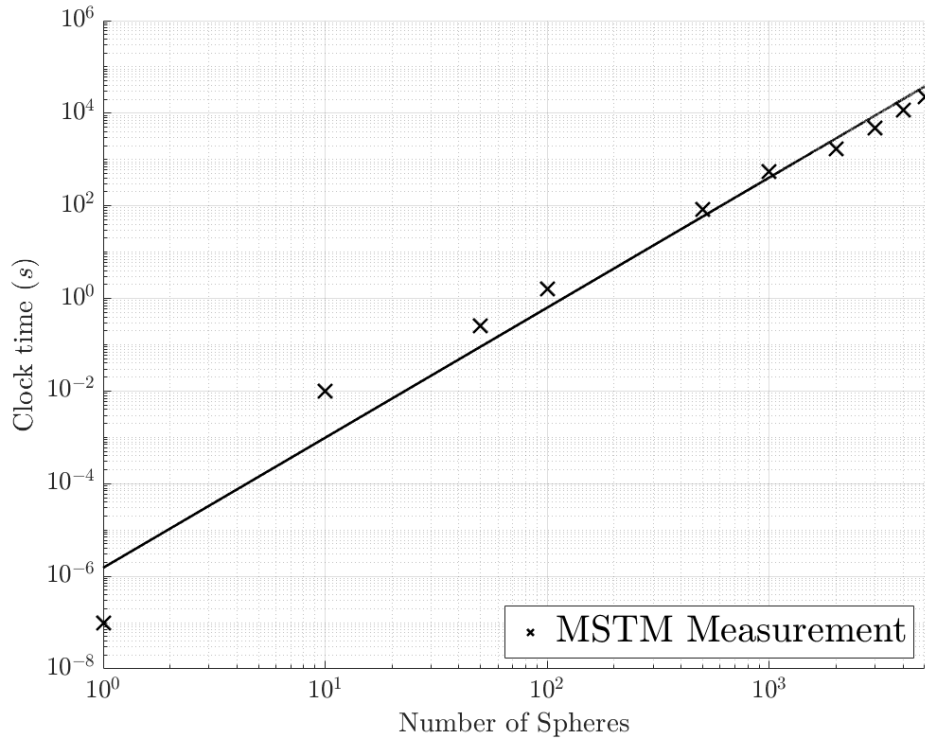


Figure 4.7: The time taken to simulate differently sized scattering domains in MSTM ($r_s = 1\mu m$, $\rho_s = 0.25\%$ and $n_s = 2.5836$). MSTM was run in parallel over four cores.

Memory usage remained $< 1\text{GB}$ at the start and for the majority of the computation - this time would have been spent performing translation calculations for the VSWFs [110]. However, during T-Matrix calculation using the bi-conjugate gradient method memory use peaked significantly to $\approx 16\text{GB}$ per core, but remained steady even if sphere number and density were increased. The near field calculation was done using our shared memory, OpenMP/MPI hybridised version of MSTM, can as such memory usage remained constant regardless of core count.

4.3 IAD Validation

Using the sphere parameters determined in Section 3.3.2.1 ($r_s = 0.5\mu m$, $n_s = 2.5836$, $\rho_s = 0.0025$) allows us to create a scattering medium where Lorenz-Mie theory predicts $\mu_s = 93.98cm^{-1}$ and $g = 0.4841$ (see Figure 3.1). In a 10,000 sphere simulation the total domain volume comes to $2.0944mm^2$ (from Equation 3.20). In Figure 4.8 we show how we can use this information to determine the optimal domain size, in which the radius is $69.3361\mu m$ and the depth is $34.6681\mu m$. The domain generated using these parameters is shown in Figure 4.9.

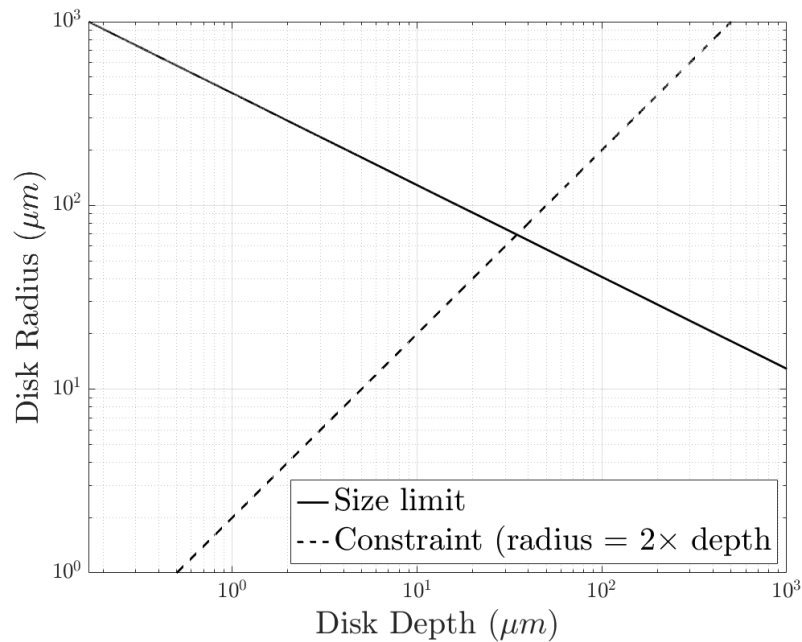


Figure 4.8: Determining the optimum radius and depth for a disk shaped scatterer. We find that using 10000 spheres of radius $r_s = 0.5\mu m$, and density $\rho_s = 0.0025$ produces a domain with a volume of $2.0944mm^2$. We then determine the radius and depth that maximise this volume while following the IAD imposed constraint that the radius must be double the depth.

We then simulated the propagation of a Gaussian beam ($\lambda = 633nm$) along the z -axis through this medium using MSTM. We measure intensity across the transmittance and reflectance planes as shown in Figure 3.2. We also plot the profile along the axis of beam propagation, we can use this to determine the ballistic light component by averaging the intensity after the scattering plane. These planes and the profile plot are found in Figure 4.10.

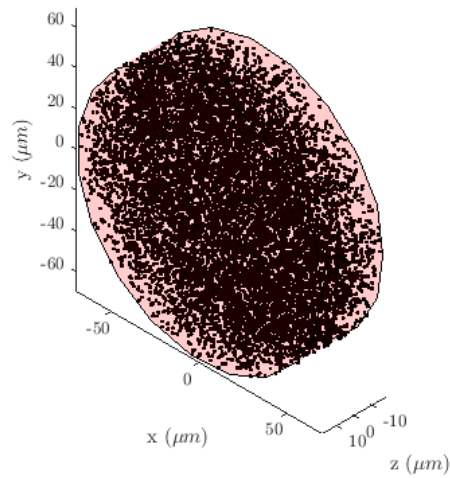


Figure 4.9: The discrete particle model used for IAD simulation. 10000 spheres are constrained by a disk of radius $69.3361\mu m$ and depth $34.6681\mu m$. Sphere density is 0.25%.

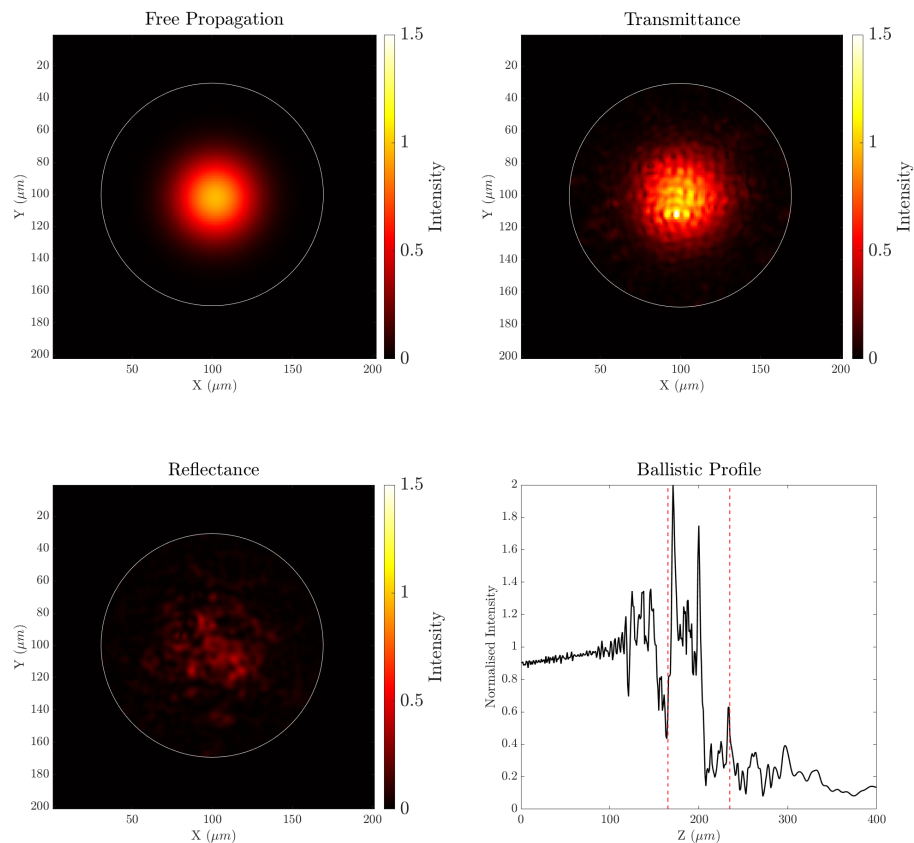


Figure 4.10: The transmittance, reflectance and ballistic profile for a Gaussian beam incident on a scattering medium calculated using MSTM. The simulated discrete particle model is shown in Figure 4.9. By normalising the intensity in the transmittance and reflectance planes by the free propagation measurement we can calculate M_T and M_R respectively. M_U is determined by averaging the intensity along the axis of beam propagation after the scattering medium (represented by the two dashed red lines). The white circles show the boundary of the scattering disk.

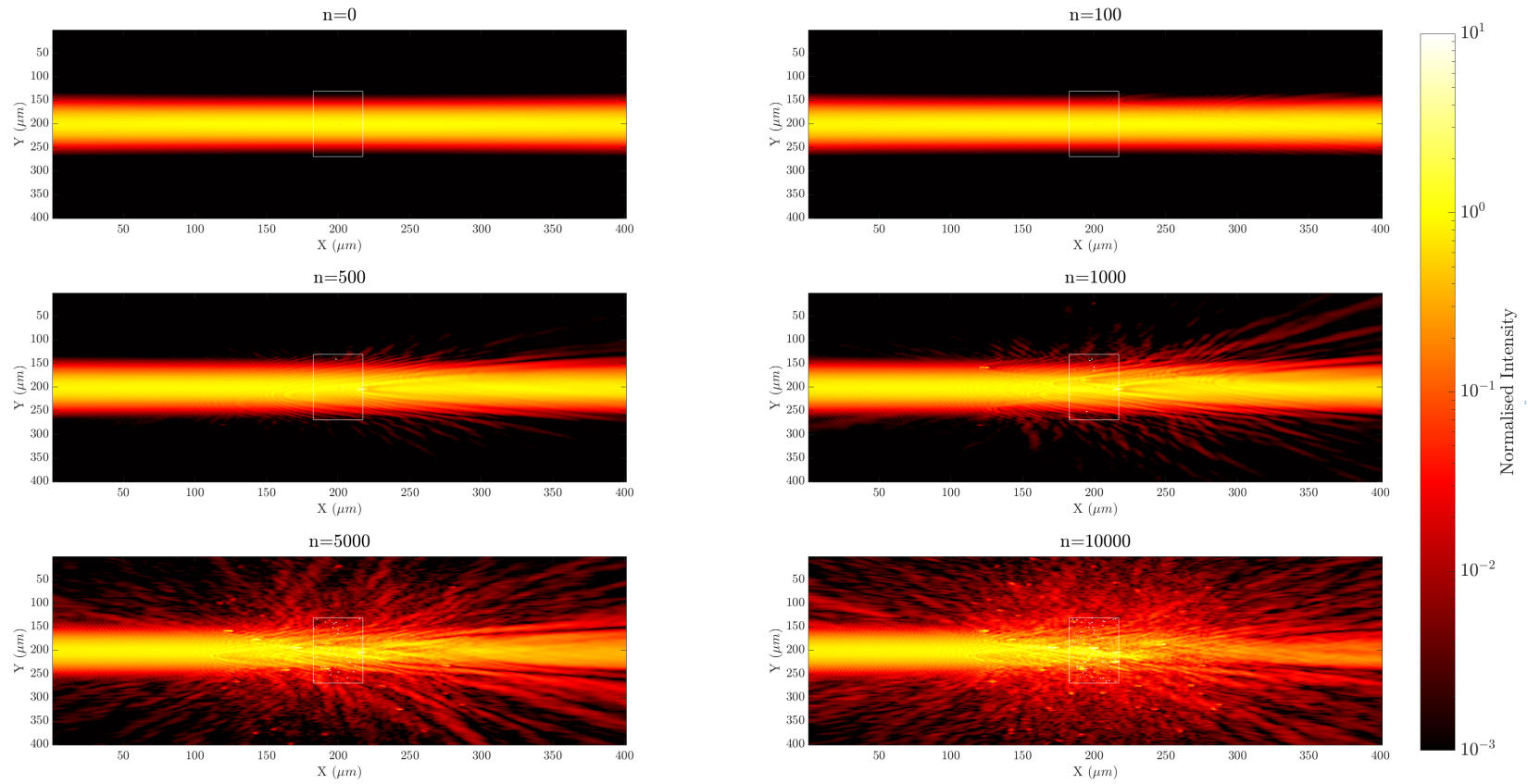


Figure 4.11: Near field intensity along the longitudinal plane for different scattering domains. Note that the proportion of light escaping from the sides of the domain increase as sphere count increases.

The accuracy of the IAD method is greatly diminished when light escape from the sides of the medium, and as such is not detected by the transmittance or reflectance planes [117]. To visualise this we create Figure 4.11 which shows the intensity along the XZ plane for different sphere counts. Notice that as the number of scatterers increases the scattering unsurprisingly becomes more pronounced. As a consequence of this, more light escapes from the sides of the computational domain.

Despite this, we found that the optical properties determined with IAD match both the values reported by MSTM and the theoretical values determined with Lorenz-Mie theory. We repeat the experiment three times, using the same geometrical constraints as Figure 4.10 but varying the position of these 10000 spheres within the constraining disk. The results are reported in Table 4.2:

Table 4.2: Optical properties of our simulation as determined by Mie theory, IAD and MSTM.

Optical property	Mie Theory	IAD	MSTM
Scattering coefficient (cm^{-1})	93.98	87.11 ± 3.31	89.56 ± 4.94
Anisotropy	0.48	$0.39 + 0.04$	0.44 ± 0.06

4.4 Speckle Generation

We conclude by using the T-Matrix method to image speckle patterns generated by propagating a plane wave through the variably sized disk scatterers where the sphere size, refractive index and density remain constant ($r_s = 0.5\mu m$, $n_s = 2.5836$, $\rho_s = 0.0025$). We image the intensity of the scattered field on the plane directly behind the scattering medium (see Figure 4.12). We find that a fully developed speckle pattern develops after approximately 500 spheres, although to verify this we plot the histogram of the 500 sphere solution and fit a Rayleigh distribution (see Figure 4.13).

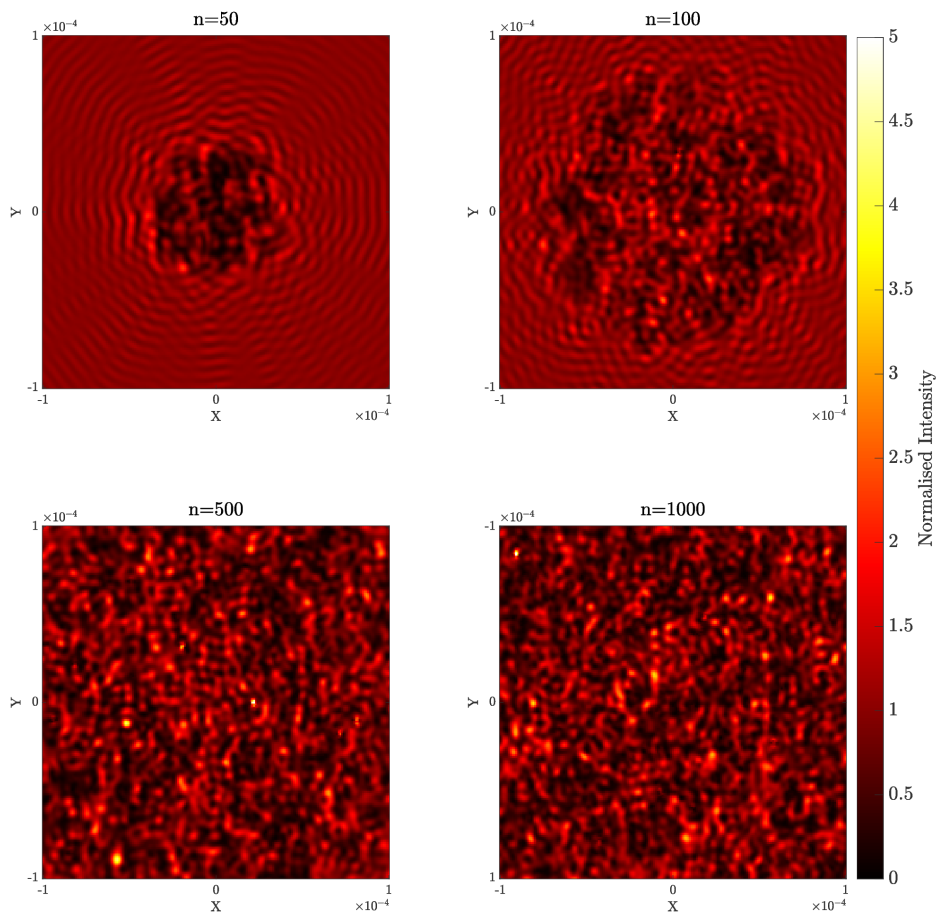


Figure 4.12: Speckle patterns generated with MSTM. Note that a lower sphere count is unable to scatter enough light to generate a fully developed speckle pattern across the entire imaging plane.

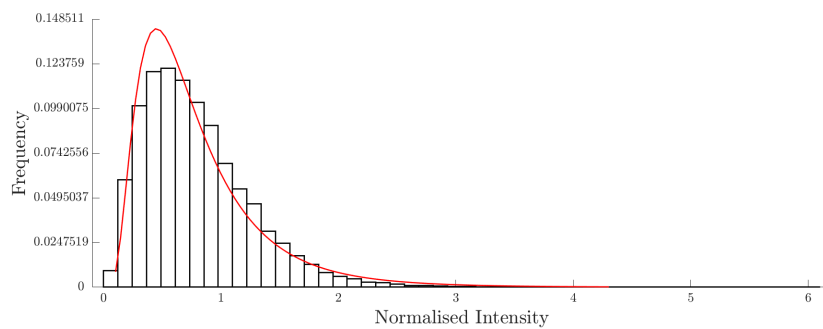


Figure 4.13: Histogram plot of the speckle pattern generated using only 500 spheres. We fit a Rayleigh distribution to validate that a fully developed speckle pattern has formed. Note that solving the T-Matrix for a 500 sphere simulation takes $< 1s$ (see Figure 4.7).

Chapter 5

Discussion

5.1 The Angular Spectrum Method

5.1.1 Diffraction Patterns

To validate our angular spectrum model we simulated Fresnel diffraction patterns of a plane wave passing through (Figure 4.1) or around (Figure 4.2) a circular aperture, before comparing the results against an existing solution based on the two-step method [130]. For both models we found that identical diffraction patterns were generated. We were also able to observe from Figure 4.2 that an Arago spot was generated - these bright spots are a direct consequence of Fresnel diffraction under certain condition [132]. The fact that we were able to replicate this well known physical phenomena is further evidence that our angular spectrum code can accurately simulate light propagation.

It is important to note that these results are not a thorough validation that our angular spectrum code can simulate the scattering of light as Yang *et al.* have proposed - only that our code has implemented the angular spectrum correctly. Unfortunately, Yang *et al.* have not made their code available [6], and the uniqueness of this angular spectrum approach to scattering makes validation difficult. In the future, it may be necessary to characterise the speckle patterns generated using this approach as a more rigorous method of validation.

5.1.2 Binary Amplitude and Phase Modulation

In Figure 4.3 we show the scattered field generated by propagating a circular aperture beam through 400 FFT-iFFT layers representing $8mm$ of scattering tissue. We use a stepwise sequential algorithm to optimise binary amplitude and phase maps that produce the optical foci seen in Figure 4.4.

One downside to this method is that the numerous Fourier and inverse Fourier transforms still take a lot of time compared to the simpler random transmission matrices currently used for algorithm comparison[20]. It took use around six hours to generate each focus seen in Figure 4.4 using only using binary modulation, computational time would increase linearly as we introduced more phase steps for each element. However, this time would decrease significantly if a faster algorithm was used (see Table 2.2 for examples).

In Table 4.1 we record the maximum focus enhancements achieved with both methods. Unfortunately, neither approach was able to match the theoretical value derived from Equation 2.1. This suggests, that although the angular spectrum method can be used to simulate a focus being generated through a scattering tissue, it does not do this in a physically realistic manner. Recall that the scattering properties of the angular spectrum medium are defined using a refractive index standard deviation, and that this deviation is determined by estimating the transport mean free path of the medium. As previously mentioned, the transport mean free path is insufficient in fully characterising the scattering properties of tissue, and as such it is impossible to fully understand exactly what material this method is actually studying. For example, a high anisotropy, low scattering coefficient and low anisotropy, high scattering coefficient material would be treated identically in this model.

This may seem like an insurmountable challenge that prevents this angular spectrum approach from being adopted to simulate wavefront shaping. However, a rigorous

first-principles approach to understanding light propagation is not the goal of this model - instead it can be used to study the impact of various confounding factors such as noise on WFS, as Yang *et al.* have done.

To this end we also notice an interesting phenomenon when looking at Table 4.1 - even though binary amplitude modulation produces a much dimmer focus than phase modulation, the light across the imaging plane is much more concentrated inside this focus, with $\eta_{\text{PBR}} = 22.85 > 11.89$. These preliminary results suggest that binary amplitude modulation might be a better fit for WFS applications that aim to improve contrast (e.g. light sheet fluorescent microscopy) as the intensity can be highly localised, while phase modulation might be more appropriate if deep tissue imaging is the goal (e.g. photoacoustic microscopy), where the main limitation is light delivery at depth.

5.2 The T-Matrix Method

5.2.1 Scaling with MSTM

Intuitively, it makes sense that the MSTM, a matrix based method, would scale nonlinearly as the size of a square matrix grows quadratically based on the number of elements. Note that our regression based formula for estimating simulation time is not generalisable to other domain geometries. The variable that has the greatest impact on computational time is not actually the number of spheres, N_s , in the simulation, but the size parameter, x . The number of linear equations that must be solved can be determined by [110]:

$$2N_s L_s (L_s + 2) \tag{5.1}$$

where, as previously mentioned, L_s is the truncation order of the VSWF expansion that is determined entirely by the size parameter according to the Wiscombe criterion (Equation 3.21). As such, the T-Matrix method is much more suited to simulating multiple small particles, on the order of $1\mu\text{m}$ for which L_0 is low.

Fortunately, memory usage remained low ($< 1\text{GB}$ per thread) during the most computationally taxing part of the simulation - the translations of the VSWF about the origin of each sphere relative to all other spheres [110]. However, memory usage did spike during the T-Matrix calculation to 16GB, suggesting there is room for further parallelisation here.

Fortunately, this T-Matrix only needs to be determined once, from then on we can use of hybrid OpenMP/MPI MSTM variant to repeatedly evaluate the near field for various incident beams using a shared memory pool.

5.3 IAD Validation

Using IAD to determine the optical properties of a scattering medium becomes less reliable the more light escapes detection. Consequently, IAD works best when the Gaussian beam width is minimised and the radius of the scattering domain is maximised. Unfortunately, these geometrical constraints run in opposition to the domains we wish to study using MSTM - by increasing the radius of the scattering domain you non-linearly decrease the depth (see Figure 4.8), and we wish to image WFS in deep tissue. There is also a limitation on how thin a Gaussian beam can be before the approximation used for the incident VSWF expansion fails ($K\omega_0 \geq 5$ where K is the wave number and ω_0 the Gaussian beam width [110]).

Fortunately, unlike the angular spectrum method, the T-Matrix approach is a rigorous, first-principles approach to simulating scattering. The macroscale optical properties of the medium are explicitly defined by the refractive index, radius and density of scatterers in the medium. This means the same values of μ_s and g measured and validated for an IAD disk like geometry would be valid for other constraining geometries (see Figure 4.5 for examples) so long as the scatterer properties remained unchanged.

From Table 4.2 we find generally good agreement with the measured optical properties of our medium as determined analytically with Lorenz-Mie theory, explicitly recorded from MSTM, or calculated using IAD. The MSTM value for the scattering coefficient matched the Mie theory and IAD values with $< 5.5\%$ difference. The variation between the anisotropy values was higher with at most a 18% difference between the analytical value and those determined with IAD. To investigate this difference, we plot the near field across the X, Z plane in Figure 4.11.

We find that a 10000 sphere simulation heavily scatters the incident Gaussian beam, leading to a higher proportion of light escaping through the sides of the scattering domain and not being detected by either the transmittance or reflectance planes. There are three possible solutions to minimise the proportion of escaping light, and improve this result:

- *Decrease the Gaussian beam width* - this increases the distance between the edge of the incident beam and the medium boundary such that less light is lost over a given domain depth. Unfortunately there is a limit on how thin the beam width can be made.
- *Increase the radius of the disk* - increasing the radius increases the distance light must travel to escape. Unfortunately, it also decreases the depth, such that there will be less scatterers directly in the path of the beam. This would increase the per sphere impact on scattering, making our measurement of μ_s and g dependent on the spatial position of individual spheres rather than the statistical description of a multi-sphere aggregate.
- *Increase both the radius and depth* - the most obvious solution is achievable by just simulating more spheres, but the non-linear scaling of the T-Matrix method make this suggestion prohibitively costly above 10000 spheres.

Rather than trying to improve the agreement between the three methods for only this given discrete particle model it may help to think of this method as a validation procedure that can come before further T-Matrix based simulation. For example,

we can use Lorenz-Mie theory to design a discrete particle model with a targeted scattering coefficient and anisotropy (see Section 3.3.2). We can then arrange these spheres to form a disk-like geometry for validation with IAD. If these results match those given directly by MSTM we can change the domain to a more convenient geometry without worry as the underlying optical properties are only dependent on scatterer refractive index, size and density which would remain constant.

5.4 Speckle Generation

We finish by imaging the speckle patterns generated using the T-Matrix method in Figure 4.12, finding that a fully developed speckle can be formed using only 500 spheres. We prove that this speckle is fully developed by noting that the intensity histogram closely follows a Rayleigh distribution 4.13. T-Matrix methods are very efficient at generating fully developed speckle patterns in very little time ($< 1s$ for a 500 sphere simulation) and as such would be a very good technique to investigate the memory effect computationally.

Chapter 6

Conclusion

If we only consider the biomedical applications, it is clear that wavefront shaping is an incredibly promising (albeit nascent) technique that has the potential to enable high contrast imaging at greater depths than currently possible. However, the inability to directly measure the scattered field inside a turbid medium, and the limitations of experimental investigation leave many unanswered questions. How exactly does shaped light propagate? What are the limits of the optical memory effect? How deep can we actually focus light? We propose that computational modelling will be able to answer many of these questions.

However, at the time of writing no researcher has proposed a rigorous computational model able to simulate wavefront shaping through deep tissue. Existing models either fail to properly characterise the optical properties of tissue (the Yang *et al.* wavefront shaping approach [6]) or are too computationally expensive for deep tissue simulation (the Kim *et al.* FDTD OCT simulation [50]).

We undertake a review of promising computational modelling techniques and evaluate their suitability for modelling wavefront shaping. We suggest that two models may be the most appropriate for different modelling objectives: the Yang *et al.* angular spectrum approach and Waterman's T-Matrix method [109].

As we have discussed previously, using the angular spectrum method to simu-

late scattering has one major disadvantage: it is impossible to fully characterise the optical properties of the simulated tissue using only the transport mean free path. Nevertheless the speed of this method make it an attractive approach to evaluating different optimisation algorithms, modulation methods. The model can also be used to study the impact different experimental variables have on efficient wavefront shaping, e.g. SLM geometry, guidestar size or even the impact of noise [6].

Further work is absolutely needed on the angular spectrum model before all this is possible. Most importantly, there must be another way to evaluate the optical properties of the model that does not rely on the transport mean free path. Studying the generated speckle patterns may be one way to understand how scattering is actually simulated with this approach.

In contrast, the T-Matrix method is much slower, and scaling limitations will likely prevent it from ever modelling centimetre-scale tissue. The method also requires that the incident field can be analytically expanded as VSWFs, making representation of arbitrary incident waves an ongoing problem [121]. However, being a discrete particle based computational technique allows the T-Matrix method to fully characterise the macro-scale optical properties of tissue through proper design of multi-sphere scattering domains. Scatterer refractive index, size and density can all be controlled to produce tissue models with a desired μ_a , μ_s and g and radius distribution can even be used to further control these optical properties [88]. This means that the T-Matrix approach is the most appropriate computational method for visualising the field inside a physically realistic scattering medium, and would be of great benefit for research into wavefront shaping or the optical memory effect.

We believe that MSTM has been sufficiently validated such that it may be used to further study wavefront shaping. The ability to simulate various incident beams using only a single T-Matrix solution makes this method well suited to this purpose. It would now be possible.

Bibliography

- [1] Lihong V Wang and Hsin-i Wu. *Biomedical optics: principles and imaging*. John Wiley & Sons, 2012.
- [2] Steven L Jacques. Optical properties of biological tissues: a review. *Physics in Medicine & Biology*, 58(11):R37, 2013.
- [3] Jung-Hoon Park, Zhipeng Yu, KyeoReh Lee, Puxiang Lai, and YongKeun Park. Perspective: Wavefront shaping techniques for controlling multiple light scattering in biological tissues: Toward in vivo applications. *APL photonics*, 3(10):100901, 2018.
- [4] Ivo M Vellekoop and AP Mosk. Focusing coherent light through opaque strongly scattering media. *Optics letters*, 32(16):2309–2311, 2007.
- [5] Roarke Horstmeyer, Haowen Ruan, and Changhuei Yang. Guidestar-assisted wavefront-shaping methods for focusing light into biological tissue. *Nature photonics*, 9(9):563–571, 2015.
- [6] Jiamiao Yang, Jingwei Li, Sailing He, and Lihong V Wang. Angular-spectrum modeling of focusing light inside scattering media by optical phase conjugation. *Optica*, 6(3):250–256, 2019.
- [7] Hilton B de Aguiar, Sylvain Gigan, and Sophie Brasselet. Enhanced nonlinear imaging through scattering media using transmission-matrix-based wavefront shaping. *Physical Review A*, 94(4):043830, 2016.
- [8] Micha Nixon, Ori Katz, Eran Small, Yaron Bromberg, Asher A Friesem, Yaron Silberberg, and Nir Davidson. Real-time wavefront shaping through

- scattering media by all-optical feedback. *Nature Photonics*, 7(11):919–924, 2013.
- [9] Changqin Ding, Chen Li, Fengyuan Deng, and Garth J Simpson. Axially-offset differential interference contrast microscopy via polarization wavefront shaping. *Optics express*, 27(4):3837–3850, 2019.
- [10] Hyeonseung Yu, Peter Lee, YoungJu Jo, KyeoReh Lee, Valery V Tuchin, Yong Jeong, and YongKeun Park. Collaborative effects of wavefront shaping and optical clearing agent in optical coherence tomography. *Journal of biomedical optics*, 21(12):121510, 2016.
- [11] Hyeonseung Yu, Jongchan Park, KyeoReh Lee, Jonghee Yoon, KyungDuk Kim, Shinwha Lee, and YongKeun Park. Recent advances in wavefront shaping techniques for biomedical applications. *Current Applied Physics*, 15(5):632–641, 2015.
- [12] Isaac Freund, Michael Rosenbluh, and Shechao Feng. Memory effects in propagation of optical waves through disordered media. *Physical review letters*, 61(20):2328, 1988.
- [13] Ivo Micha Vellekoop and AP Mosk. Universal optimal transmission of light through disordered materials. *Physical review letters*, 101(12):120601, 2008.
- [14] Ivo M Vellekoop. Feedback-based wavefront shaping. *Optics express*, 23(9):12189–12206, 2015.
- [15] Ivo Micha Vellekoop, EG Van Putten, A Lagendijk, and AP Mosk. Demixing light paths inside disordered metamaterials. *Optics express*, 16(1):67–80, 2008.
- [16] Puxiang Lai, Lidai Wang, Jian Wei Tay, and Lihong V Wang. Photoacoustically guided wavefront shaping for enhanced optical focusing in scattering media. *Nature photonics*, 9(2):126–132, 2015.

- [17] Ori Katz, Eran Small, Yefeng Guan, and Yaron Silberberg. Noninvasive non-linear focusing and imaging through strongly scattering turbid layers. *Optica*, 1(3):170–174, 2014.
- [18] Muhammad Mohsin Qureshi, Joshua Brake, Hee-Jae Jeon, Haowen Ruan, Yan Liu, Abdul Mohaimen Safi, Tae Joong Eom, Changhuei Yang, and Eui-heon Chung. In vivo study of optical speckle decorrelation time across depths in the mouse brain. *Biomedical optics express*, 8(11):4855–4864, 2017.
- [19] Omer Tzang, Eyal Niv, Sakshi Singh, Simon Labouesse, Greg Myatt, and Rafael Piestun. Wavefront shaping in complex media with a 350 khz modulator via a 1d-to-2d transform. *Nature Photonics*, 13(11):788–793, 2019.
- [20] Zahra Fayyaz, Nafiseh Mohammadian, M Reza Rahimi Tabar, Rayyan Manwar, and Kamran Avanaki. A comparative study of optimization algorithms for wavefront shaping. *Journal of Innovative Optical Health Sciences*, 12(04):1942002, 2019.
- [21] Zahra Fayyaz, Nafiseh Mohammadian, and Mohammad RN Avanaki. Comparative assessment of five algorithms to control an slm for focusing coherent light through scattering media. In *Photons Plus Ultrasound: Imaging and Sensing 2018*, volume 10494, page 104946I. International Society for Optics and Photonics, 2018.
- [22] JV Thompson, BH Hokr, and VV Yakovlev. Optimization of focusing through scattering media using the continuous sequential algorithm. *Journal of modern optics*, 63(1):80–84, 2016.
- [23] Ivo Micha Vellekoop and AP Mosk. Phase control algorithms for focusing light through turbid media. *Optics communications*, 281(11):3071–3080, 2008.
- [24] SM Popoff, G Lerosey, R Carminati, M Fink, AC Boccara, and S Gigan. Measuring the transmission matrix in optics: an approach to the study and

- control of light propagation in disordered media. *Physical review letters*, 104(10):100601, 2010.
- [25] Donald B Conkey, Albert N Brown, Antonio M Caravaca-Aguirre, and Rafael Piestun. Genetic algorithm optimization for focusing through turbid media in noisy environments. *Optics express*, 20(5):4840–4849, 2012.
- [26] Zahid Yaqoob, Demetri Psaltis, Michael S Feld, and Changhuei Yang. Optical phase conjugation for turbidity suppression in biological samples. *Nature photonics*, 2(2):110–115, 2008.
- [27] Meng Cui and Changhuei Yang. Implementation of a digital optical phase conjugation system and its application to study the robustness of turbidity suppression by phase conjugation. *Optics express*, 18(4):3444–3455, 2010.
- [28] Chia-Lung Hsieh, Ye Pu, Rachel Grange, Grégoire Laporte, and Demetri Psaltis. Imaging through turbid layers by scanning the phase conjugated second harmonic radiation from a nanoparticle. *Optics express*, 18(20):20723–20731, 2010.
- [29] Ivo M Vellekoop, Meng Cui, and Changhuei Yang. Digital optical phase conjugation of fluorescence in turbid tissue. *Applied physics letters*, 101(8):081108, 2012.
- [30] Zhipeng Yu, Jiangtao Huangfu, Fangyuan Zhao, Meiyun Xia, Xi Wu, Xufeng Niu, Deyu Li, Puxiang Lai, and Daifa Wang. Time-reversed magnetically controlled perturbation (trmcp) optical focusing inside scattering media. *Scientific reports*, 8(1):1–8, 2018.
- [31] GD Mahan, WE Engler, JJ Tiemann, and E Uzgiris. Ultrasonic tagging of light: theory. *Proceedings of the National Academy of Sciences*, 95(24):14015–14019, 1998.

- [32] Xiao Xu, Honglin Liu, and Lihong V Wang. Time-reversed ultrasonically encoded optical focusing into scattering media. *Nature photonics*, 5(3):154–157, 2011.
- [33] Benjamin Judkewitz, Ying Min Wang, Roarke Horstmeyer, Alexandre Mathy, and Changhuei Yang. Speckle-scale focusing in the diffusive regime with time reversal of variance-encoded light (trove). *Nature photonics*, 7(4):300–305, 2013.
- [34] Haowen Ruan, Mooseok Jang, and Changhuei Yang. Optical focusing inside scattering media with time-reversed ultrasound microbubble encoded light. *Nature communications*, 6(1):1–8, 2015.
- [35] Cheng Ma, Xiao Xu, Yan Liu, and Lihong V Wang. Time-reversed adapted-perturbation (trap) optical focusing onto dynamic objects inside scattering media. *Nature photonics*, 8(12):931–936, 2014.
- [36] Edward Haojiang Zhou, Haowen Ruan, Changhuei Yang, and Benjamin Judkewitz. Focusing on moving targets through scattering samples. *Optica*, 1(4):227–232, 2014.
- [37] Minghua Xu and Lihong V Wang. Photoacoustic imaging in biomedicine. *Review of scientific instruments*, 77(4):041101, 2006.
- [38] Lihong V Wang and Song Hu. Photoacoustic tomography: in vivo imaging from organelles to organs. *science*, 335(6075):1458–1462, 2012.
- [39] Paul Beard. Biomedical photoacoustic imaging. *Interface focus*, 1(4):602–631, 2011.
- [40] Donald B Conkey, Antonio M Caravaca-Aguirre, Jake D Dove, Hengyi Ju, Todd W Murray, and Rafael Piestun. Super-resolution photoacoustic imaging through a scattering wall. *Nature communications*, 6(1):1–7, 2015.

- [41] Puxiang Lai, Lidai Wang, Jian Wei Tay, and Lihong V Wang. Nonlinear photoacoustic wavefront shaping (paws) for single speckle-grain optical focusing in scattering media. *arXiv preprint arXiv:1402.0816*, 2014.
- [42] Thomas Chaigne, Jérôme Gateau, Ori Katz, Emmanuel Bossy, and Sylvain Gigan. Light focusing and two-dimensional imaging through scattering media using the photoacoustic transmission matrix with an ultrasound array. *Optics letters*, 39(9):2664–2667, 2014.
- [43] Thomas Chaigne, Ori Katz, A Claude Boccara, Mathias Fink, Emmanuel Bossy, and Sylvain Gigan. Controlling light in scattering media non-invasively using the photoacoustic transmission matrix. *Nature Photonics*, 8(1):58–64, 2014.
- [44] Dan P Popescu, Costel Flueraru, Youxin Mao, Shoude Chang, John Disano, Sherif Sherif, Michael G Sowa, et al. Optical coherence tomography: fundamental principles, instrumental designs and biomedical applications. *Biophysical reviews*, 3(3):155, 2011.
- [45] James G Fujimoto, Costas Pitris, Stephen A Boppart, and Mark E Brezinski. Optical coherence tomography: an emerging technology for biomedical imaging and optical biopsy. *Neoplasia*, 2(1-2):9–25, 2000.
- [46] David Huang, Eric A Swanson, Charles P Lin, Joel S Schuman, William G Stinson, Warren Chang, Michael R Hee, Thomas Flotte, Kenton Gregory, Carmen A Puliafito, et al. Optical coherence tomography. *science*, 254(5035):1178–1181, 1991.
- [47] Hyeonseung Yu, Peter Lee, KyeoReh Lee, Jaeduck Jang, Jaeguyn Lim, Wooyoung Jang, Yong Jeong, and YongKeun Park. In vivo deep tissue imaging using wavefront shaping optical coherence tomography. *Journal of biomedical optics*, 21(10):101406, 2016.

- [48] Adolf F Fercher, Wolfgang Drexler, Christoph K Hitzenberger, and Theo Lasser. Optical coherence tomography-principles and applications. *Reports on progress in physics*, 66(2):239, 2003.
- [49] Hyeonseung Yu, Jaeduck Jang, Jaeguyn Lim, Jung-Hoon Park, Wooyoung Jang, Ji-Yeun Kim, and YongKeun Park. Depth-enhanced 2-d optical coherence tomography using complex wavefront shaping. *Optics express*, 22(7):7514–7523, 2014.
- [50] Jong Uk Kim, Hyun Choi, YongKeun Park, and Jonghwa Shin. Finite-difference time-domain analysis of increased penetration depth in optical coherence tomography by wavefront shaping. *Biomedical Optics Express*, 9(8):3883–3897, 2018.
- [51] Fritjof Helmchen and Winfried Denk. Deep tissue two-photon microscopy. *Nature methods*, 2(12):932–940, 2005.
- [52] Jianyong Tang, Ronald N Germain, and Meng Cui. Superpenetration optical microscopy by iterative multiphoton adaptive compensation technique. *Proceedings of the National Academy of Sciences*, 109(22):8434–8439, 2012.
- [53] Peter A Santi. Light sheet fluorescence microscopy: a review. *Journal of Histochemistry & Cytochemistry*, 59(2):129–138, 2011.
- [54] Joel Kubby, Sylvain Gigan, and Meng Cui. *Wavefront shaping for biomedical imaging*. Cambridge University Press, 2019.
- [55] Heather Isla Campbell Dalgarno, T Čižmár, Tom Vettenburg, Jonathan Nylk, Frank J Gunn-Moore, and Kishan Dholakia. Wavefront corrected light sheet microscopy in turbid media. *Applied Physics Letters*, 100(19):191108, 2012.
- [56] Jale Schneider and Christof M Aegerter. Dynamic light sheet generation and fluorescence imaging behind turbid media. *Journal of the European Optical Society-Rapid Publications*, 14(1):7, 2018.

- [57] Jayan Mannath and Matthew Banks. Emerging technologies in endoscopic imaging. *F1000 medicine reports*, 4, 2012.
- [58] Ioannis N Papadopoulos, Salma Farahi, Christophe Moser, and Demetri Psaltis. Focusing and scanning light through a multimode optical fiber using digital phase conjugation. *Optics express*, 20(10):10583–10590, 2012.
- [59] Ioannis N Papadopoulos, Salma Farahi, Christophe Moser, and Demetri Psaltis. High-resolution, lensless endoscope based on digital scanning through a multimode optical fiber. *Biomedical optics express*, 4(2):260–270, 2013.
- [60] Donggyu Kim, Jungho Moon, Moonseok Kim, Taeseok Daniel Yang, Jaisoon Kim, Euiheon Chung, and Wonshik Choi. Pixelation-free and real-time endoscopic imaging through a fiber bundle. *arXiv preprint arXiv:1308.6719*, 2013.
- [61] Thomas J Dougherty, Charles J Gomer, Barbara W Henderson, Giulio Jori, David Kessel, Mladen Korbelik, Johan Moan, and Qian Peng. Photodynamic therapy. *JNCI: Journal of the national cancer institute*, 90(12):889–905, 1998.
- [62] Dennis EJGJ Dolmans, Dai Fukumura, and Rakesh K Jain. Photodynamic therapy for cancer. *Nature reviews cancer*, 3(5):380–387, 2003.
- [63] Matthew R Banghart, Matthew Volgraf, and Dirk Trauner. Engineering light-gated ion channels. *Biochemistry*, 45(51):15129–15141, 2006.
- [64] Lief Fenno, Ofer Yizhar, and Karl Deisseroth. The development and application of optogenetics. *Annual review of neuroscience*, 34, 2011.
- [65] Yusuf Tufail, Anna Yoshihiro, Sandipan Pati, Monica M Li, and William J Tyler. Ultrasonic neuromodulation by brain stimulation with transcranial ultrasound. *nature protocols*, 6(9):1453–1470, 2011.

- [66] Jonghee Yoon, Minji Lee, KyeoReh Lee, Nury Kim, Jin Man Kim, Jongchan Park, Hyeonseung Yu, Chulhee Choi, Won Do Heo, and YongKeun Park. Optogenetic control of cell signaling pathway through scattering skull using wavefront shaping. *Scientific reports*, 5:13289, 2015.
- [67] Arthur Ashkin, James M Dziedzic, John E Bjorkholm, and Steven Chu. Observation of a single-beam gradient force optical trap for dielectric particles. *Optics letters*, 11(5):288–290, 1986.
- [68] Michael A Taylor, Muhammad Waleed, Alexander B Stilgoe, Halina Rubinsztein-Dunlop, and Warwick P Bowen. Enhanced optical trapping via structured scattering. *Nature Photonics*, 9(10):669–673, 2015.
- [69] Michael A Taylor. Optimizing phase to enhance optical trap stiffness. *Scientific reports*, 7(1):1–10, 2017.
- [70] Max Born and Emil Wolf. *Principles of optics: electromagnetic theory of propagation, interference and diffraction of light*. Elsevier, 2013.
- [71] Jung-Hoon Park, Chunghyun Park, Yong-Hoon Cho, and YongKeun Park. Scattering super-lens: subwavelength light focusing and imaging via wavefront shaping in complex media. In *CLEO: QELS Fundamental Science*, pages FW1C–6. Optical Society of America, 2014.
- [72] Ivo M Vellekoop, Aart Lagendijk, and AP Mosk. Exploiting disorder for perfect focusing. *Nature photonics*, 4(5):320–322, 2010.
- [73] Bahram Javidi, Artur Carnicer, Masahiro Yamaguchi, Takanori Nomura, Elisabet Pérez-Cabré, María S Millán, Naveen K Nishchal, Roberto Torroba, John Fredy Barrera, Wenqi He, et al. Roadmap on optical security. *Journal of Optics*, 18(8):083001, 2016.
- [74] Sebastianus A Goorden, Marcel Horstmann, Allard P Mosk, Boris Škorić, and Pepijn WH Pinkse. Quantum-secure authentication of a physical unclonable key. *Optica*, 1(6):421–424, 2014.

- [75] William K Wootters and Wojciech H Zurek. A single quantum cannot be cloned. *Nature*, 299(5886):802–803, 1982.
- [76] Meihua Liao, Dajiang Lu, Wenqi He, and Xiang Peng. Optical cryptanalysis method using wavefront shaping. *IEEE Photonics Journal*, 9(1):1–13, 2017.
- [77] Vincent WS Chan. Free-space optical communications. *Journal of Lightwave technology*, 24(12):4750–4762, 2006.
- [78] Marzieh Najafi, Bernhard Schmauss, and Robert Schober. Intelligent reconfigurable reflecting surfaces for free space optical communications. *arXiv preprint arXiv:2005.04499*, 2020.
- [79] Nadège Kaina, Matthieu Dupré, Geoffroy Lerosey, and Mathias Fink. Shaping complex microwave fields in reverberating media with binary tunable metasurfaces. *Scientific reports*, 4(1):1–8, 2014.
- [80] Zizheng Cao, Xuebing Zhang, Gerwin Osnabrugge, Juhao Li, Ivo M Vellekoop, and Antonius MJ Koonen. Reconfigurable beam system for non-line-of-sight free-space optical communication. *Light: Science & Applications*, 8(1):1–9, 2019.
- [81] LV Wang and DA Zimnyakov. *Optical polarization in biomedical applications*. Springer, 2006.
- [82] JM Schmitt and G Kumar. Turbulent nature of refractive-index variations in biological tissue. *Optics letters*, 21(16):1310–1312, 1996.
- [83] Valery V Tuchin et al. *Tissue optics*. Society of Photo-Optical Instrumentation Engineers (SPIE), 2015.
- [84] Howard R Gordon. Light scattering and absorption by randomly-oriented cylinders: dependence on aspect ratio for refractive indices applicable for marine particles. *Optics express*, 19(5):4673–4691, 2011.

- [85] Tom Rother, Karsten Schmidt, Jochen Wauer, Valery Shcherbakov, and Jean-Francois Gayet. Light scattering on chebyshev particles of higher order. *Applied optics*, 45(23):6030–6037, 2006.
- [86] Hendrik Christoffel Hulst and Hendrik C van de Hulst. *Light scattering by small particles*. Courier Corporation, 1981.
- [87] GC Beck, N Akgün, A Rück, and R Steiner. Design and characterisation of a tissue phantom system for optical diagnostics. *Lasers in medical science*, 13(3):160–171, 1998.
- [88] Joseph M Schmitt and Gitesh Kumar. Optical scattering properties of soft tissue: a discrete particle model. *Applied optics*, 37(13):2788–2797, 1998.
- [89] P Sumithra and D Thiripurasundari. Review on computational electromagnetics. *Advanced Electromagnetics*, 6(1):42–55, 2017.
- [90] Kane Yee. Numerical solution of initial boundary value problems involving maxwell’s equations in isotropic media. *IEEE Transactions on antennas and propagation*, 14(3):302–307, 1966.
- [91] Allen Taflove and Susan C Hagness. *Computational electrodynamics: the finite-difference time-domain method*. Artech house, 2005.
- [92] Allen Taflove and Susan C Hagness. Computational electromagnetics: the finite-difference time-domain method. *Artech House, Boston*, pages 149–161, 1995.
- [93] David B Davidson. *Computational electromagnetics for RF and microwave engineering*. Cambridge University Press, 2010.
- [94] Jean-Pierre Berenger et al. A perfectly matched layer for the absorption of electromagnetic waves. *Journal of computational physics*, 114(2):185–200, 1994.

- [95] Qing H Liu. The pseudospectral time-domain (pstd) method: A new algorithm for solutions of maxwell's equations. In *IEEE Antennas and Propagation Society International Symposium 1997. Digest*, volume 1, pages 122–125. IEEE, 1997.
- [96] Qing H Liu. The pstd algorithm: A time-domain method requiring only two cells per wavelength. *Microwave and optical technology letters*, 15(3):158–165, 1997.
- [97] Krishnaswamy Sankaran. Are you using the right tools in computational electromagnetics? *Engineering Reports*, 1(3):e12041, 2019.
- [98] Jian-Ming Jin. *The finite element method in electromagnetics*. John Wiley & Sons, 2015.
- [99] Anders Bondeson, Thomas Rylander, and Pär Ingelström. *Computational electromagnetics*. Springer, 2012.
- [100] Jin-Fa Lee, Robert Lee, and Andreas Cangellaris. Time-domain finite-element methods. *IEEE transactions on antennas and propagation*, 45(3):430–442, 1997.
- [101] Martin Costabel. *Principles of boundary element methods*. Techn. Hochsch., Fachbereich Mathematik, 1986.
- [102] Scott A Prahl. A monte carlo model of light propagation in tissue. In *Dosimetry of laser radiation in medicine and biology*, volume 10305, page 1030509. International Society for Optics and Photonics, 1989.
- [103] Caigang Zhu and Quan Liu. Review of monte carlo modeling of light transport in tissues. *Journal of biomedical optics*, 18(5):050902, 2013.
- [104] Chen Bar, Marina Alterman, Ioannis Gkioulekas, and Anat Levin. A monte carlo framework for rendering speckle statistics in scattering media. *ACM Transactions on Graphics (TOG)*, 38(4):1–22, 2019.

- [105] Bruce T Draine and Piotr J Flatau. Discrete-dipole approximation for scattering calculations. *Josa a*, 11(4):1491–1499, 1994.
- [106] Maxim A Yurkin and Alfons G Hoekstra. The discrete dipole approximation: an overview and recent developments. *Journal of Quantitative Spectroscopy and Radiative Transfer*, 106(1-3):558–589, 2007.
- [107] Brian W Pogue and Michael S Patterson. Review of tissue simulating phantoms for optical spectroscopy, imaging and dosimetry. *Journal of biomedical optics*, 11(4):041102, 2006.
- [108] Joseph W Goodman. *Introduction to Fourier optics*. Roberts and Company Publishers, 2005.
- [109] PC Waterman. Matrix formulation of electromagnetic scattering. *Proceedings of the IEEE*, 53(8):805–812, 1965.
- [110] DW Mackowski and MI Mishchenko. A multiple sphere t-matrix fortran code for use on parallel computer clusters. *Journal of Quantitative Spectroscopy and Radiative Transfer*, 112(13):2182–2192, 2011.
- [111] Michael I Mishchenko, Larry D Travis, and Daniel W Mackowski. T-matrix computations of light scattering by nonspherical particles: a review. *Journal of Quantitative Spectroscopy and Radiative Transfer*, 55(5):535–575, 1996.
- [112] Thomas Wriedt and Ute Comberg. Comparison of computational scattering methods. *Journal of Quantitative Spectroscopy and Radiative Transfer*, 60(3):411–423, 1998.
- [113] KM Yoo, Feng Liu, and RR Alfano. When does the diffusion approximation fail to describe photon transport in random media? *Physical review letters*, 64(22):2647, 1990.
- [114] G Gouesbet, JA Lock, and G Gréhan. Generalized lorenz–mie theories and description of electromagnetic arbitrary shaped beams: localized approxi-

- mations and localized beam models, a review. *Journal of Quantitative Spectroscopy and Radiative Transfer*, 112(1):1–27, 2011.
- [115] Yunqi Luo, Huanhao Li, Ruochong Zhang, Puxiang Lai, and Yuanjin Zheng. Deep learning assisted optical wavefront shaping in disordered medium. In *Adaptive Optics and Wavefront Control for Biological Systems V*, volume 10886, page 1088612. International Society for Optics and Photonics, 2019.
- [116] SF Cheng, HH Li, YQ Luo, YJ Zheng, and PX Lai. Artificial intelligence-assisted light control and computational imaging through scattering media. *Journal of innovative optical health sciences*, 2019.
- [117] Scott Prael. Everything i think you should know about inverse adding-doubling. *Oregon Medical Laser Center, St. Vincent Hospital*, pages 1–74, 2011.
- [118] Daniel W Mackowski. Calculation of total cross sections of multiple-sphere clusters. *JOSA A*, 11(11):2851–2861, 1994.
- [119] Michael I Mishchenko, Larry D Travis, and Andrew A Lacis. *Scattering, absorption, and emission of light by small particles*. Cambridge university press, 2002.
- [120] K Aydin and A Hizal. On the completeness of the spherical vector wave functions. *Journal of mathematical analysis and applications*, 117(2):428–440, 1986.
- [121] A Doicu and T Wriedt. Computation of the beam-shape coefficients in the generalized lorenz–mie theory by using the translational addition theorem for spherical vector wave functions. *Applied Optics*, 36(13):2971–2978, 1997.
- [122] Boris D Lubachevsky and Frank H Stillinger. Geometric properties of random disk packings. *Journal of statistical Physics*, 60(5-6):561–583, 1990.
- [123] J Rs DeVore. Refractive indices of rutile and sphalerite. *JOSA*, 41(6):416–419, 1951.

- [124] Gerard L Coté, LiHong V Wang, and Sohi Rastegar. Biomedical optics and lasers. In *Introduction to Biomedical Engineering*, pages 977–1043. Elsevier, 2005.
- [125] Craig F Bohren and Donald R Huffman. *Absorption and scattering of light by small particles*. John Wiley & Sons, 2008.
- [126] Peter Pacheco. *An introduction to parallel programming*. Elsevier, 2011.
- [127] Amos Egel, Lorenzo Pattelli, Giacomo Mazzamuto, Diederik S Wiersma, and Uli Lemmer. Celes: Cuda-accelerated simulation of electromagnetic scattering by large ensembles of spheres. *Journal of Quantitative Spectroscopy and Radiative Transfer*, 199:103–110, 2017.
- [128] Dag Wieers. Dstat: Versatile resource statistics tool. *online*] <http://dag.wieers/home-made/dstat/>(accessed September 2020), 2013.
- [129] Klaus D Mielenz. Algorithms for fresnel diffraction at rectangular and circular apertures. *Journal of research of the National Institute of Standards and Technology*, 103(5):497, 1998.
- [130] J.D. Schmidt. *Numerical Simulation of Optical Wave Propagation with Examples in MATLAB*. Press monograph. SPIE, 2010.
- [131] Scott Prahl. Optical property measurements using the inverse adding-doubling program. *Oregon Medical Laser Center, St. Vincent Hospital, 9205*, 1999.
- [132] E. Hecht. *Optics*. Always learning. Pearson, 2016.